Department of Physics and Astronomy
Heidelberg University

Bachelor Thesis in Physics
submitted by

Moritz Raab

born in Sinsheim (Germany)

1998

Optical properties and pulse shape discrimination of safe liquid scintillators

Zusammenfassung:

In der Teilchenphysik, speziell im Bereich der Neutrinophysik, gibt es steigende Nachfrage nach sicheren Flüssigszintillatoren für große Detektoren. Deshalb wurden innerhalb dieser Arbeit unterschiedliche Szintillatoren untersucht, die sich vor allem durch einen hohen Flammpunkt und niedrigen Dampfdruck auszeichnen. Die optischen Eigenschaften der betrachteten Lösungsmittel wurden durch die Wahl unterschiedlicher Wellenlängenschieber und durch Variation der Konzentration optimiert. Dafür wurde die Lichtausbeute, Absorptionslänge sowie die Fähigkeit zur Unterscheidung unterschiedlicher ionisierender Teilchen (PSD) der Szintillatorproben bestimmt. Dabei konnten sich drei Szintillatorproben basierend auf DIN, LAB und Silikonöl hervorheben. Der DIN basierte Szintillator zeichnet sich durch seine herausragende Lichtausbeute und PSD aus, hat jedoch eine relativ geringe Absorptionslänge. Der LAB basierte Szintillator hingegen hat eine mehr als fünf Mal größere Absorptionslänge als DIN, jedoch eine geringere Lichtausbeute sowie schlechtere PSD. Der Silikonöl basierte Szintillator besitzt eine minimal schlechtere Lichtausbeute und PSD als LAB, jedoch charakterisiert sich dieser durch einen sehr hohen Flammpunkt sowie sehr geringen Dampfdruck selbst im Vergleich zu anderen sicheren Flüssigszintillatoren. Darüberhinaus ist er chemisch inert, problemlos entsorgbar und besitzt kein GHS Piktogramm.

Abstract:

In particle physics, especially in neutrino physics, there is rising demand for safe liquid scintillators in large detectors. Therefore, different scintillators, which are characterised by a high flash point and low vapour pressure, were studied in context of this work. The optical properties of different safe solvent were optimized by the selection of different wavelength shifters and variation of their concentration. In particular, the light yield, attenuation length and the capability of Pulse Shape Discrimination (PSD) of different scintillator samples were determined. In this context we found three promising scintillator samples based on DIN, LAB and silicone oil. The DIN based scintillator has an outstanding light yield and PSD, but a relative low attenuation length. The LAB based scintillator on the other hand has a more than five times larger attenuation length than DIN, but a lower light yield and PSD. The silicone oil based scintillator has a slightly worse light yield and PSD than LAB, but is characterised by a very high flash point and very low vapour pressure even compared to other safe scintillators. Moreover, it is chemical inert, simple disposable and classified with no GHS pictogram.

This Bachelor Thesis has been carried out by Moritz Raab at the
Max-Planck-Institut für Kernphysik in Heidelberg
under the supervision of
Prof. Dr. Dr. h.c. Manfred Lindner

Contents

Part I

Organic liquid scintillators

1 Interaction of particles with matter

Scintillators are among the classical materials used to detect ionising radiation [1]. The detection is based on the scintillation effect, which corresponds to luminescence caused by the interaction of ionising radiation with the scintillator material. There are two major types of scintillators: organic and inorganic scintillators. We focus on organic liquid scintillators, which have the advantage of providing high flexibility, availability of several purification techniques and cost-effectiveness. To understand the energy transfer mechanisms (chapter 2) of an organic liquid scintillator, one first has to understand how particles interact with matter.

1.1 Charged particles

1.1.1 Ionisation

Ionisation and excitation (section 1.4) are among the most important energy losses by charged particles. The average energy loss per unit length $\frac{dE}{dx}$ in a homogeneous material is well described by the Bethe-Bloch formula [2].

$$-\frac{dE}{dx} \simeq \rho D \left(\frac{Z}{A}\right) \frac{z_p^2}{\beta^2} \left[\frac{1}{2} \ln\left(\frac{2m_e c^2 \beta^2 \gamma^2}{I}\right) - \beta^2 - \frac{\delta(\beta, \rho)}{2}\right] \tag{1.1}$$

where ρ is the density in g/cm^3, Z and A are the atomic and mass number of the material, z_p is the charge of the incoming particle in units of electron charge, $D \simeq 0.307$ MeV cm^2/g, m_e the mass of an electron, c the speed of light, I the mean excitation energy in the material, $\beta = v/c$ with velocity v of the particle, $\gamma = \frac{1}{\sqrt{1-\beta^2}}$ the Lorentz factor and δ a correction term that becomes important at high energies.

The energy loss by ionisation and excitation (1.1) is to first order approximation independent of the particles mass for $m \gg m_e$, proportional to Z/A and nearly constant for $\beta > 0.96$ due to the logarithmic scaling.

The Bethe-Bloch formula can not describe electrons or positrons due to the small mass and indistinguishably of electrons from the orbital electrons.

Instead, the energy loss of electrons and positrons can be described by the Berger-Seltzer formula [3]:

$$-\frac{dE}{dx} = 2\pi r_e^2 n_e \frac{m_e c^2}{1-\gamma^{-2}} \left[\ln\left(2(\gamma+1)\frac{m_e^2 c^4}{I^2}\right) + \frac{1}{\gamma^2} + \ln\left(\frac{\tau^2}{4}\right) + \frac{\tau^2}{8\gamma^2} - \frac{2\tau+1}{\gamma^2}\ln(2) \right] \tag{1.2}$$

where r_e is the classical electron radius, $\tau = \gamma - 1$ and n_e the electron density.

1.1.2 Cherenkov radiation

Cherenkov radiation occurs when a charged particle moves through a medium with a higher velocity than the speed of light in that medium [2]. The light is emitted in a cone at an angle θ_c from the direction of the particle (Figure 1.1).

$$\cos\theta_c = \frac{1}{n\beta} \tag{1.3}$$

The total energy loss due to Cherenkov radiation only plays a minor role compared to excitation and ionisation. Typical contribution to the total scintillator light for a few MeV electron is in the region of a few percent.

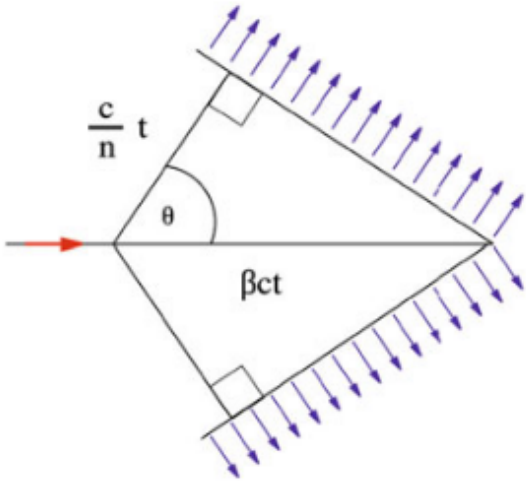

Figure 1.1: Cherenkov radiation caused by a charged particle [2]

1.1.3 Bremsstrahlung

In classical electromagnetism a charged particle undergoing acceleration radiates electromagnetic waves with an intensity proportional to the square of the acceleration. Charged particles that are traversing a material get accelerated by the

electric fields of the material and therefore emit photons. This radiation is called bremsstrahlung. Because the emitted energy is proportional to the inverse of the mass squared, this effect becomes more important for light particles. Therefore, bremsstrahlung is particularly relevant for electrons and positrons, where the average energy loss by radiation for high energies ($E \gg m_e c^2$) can be approximated by [2]:

$$\frac{dE}{dx} \simeq -\frac{E}{X_0} \tag{1.4}$$

where X_0 is the radiation length which is characteristic for the material. A good approximation for $Z > 4$ is given by

$$\frac{1}{X_0} = 4\left(\frac{\hbar}{m_e c}\right)^2 Z(Z+1)\alpha^3 n_a \ln\left(\frac{183}{Z^{1/3}}\right) \tag{1.5}$$

where $\hbar$ is the reduced Planck constant, $\alpha = \frac{e^2}{4\pi}$ with elementary charge e and n_a is the density of atoms per cubic centimetre in the medium. The equation 1.4 shows that the total average energy loss by radiation of bremsstrahlung increases linearly with the energy of the particle.

1.2 Photons

Photons mostly interact with matter via the photoelectric effect, Compton scattering and electron–positron pair production [2]. Figure 1.2 shows the mass attenuation coefficient, which is the cross section per gram of material, as a function of photon energy. It shows how the different effects add up to the total mass attenuation coefficient for different energies of the photon.

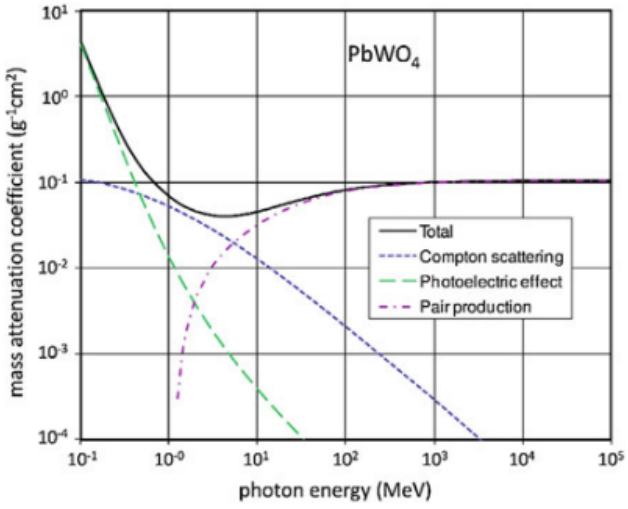

Figure 1.2: Photon interaction with Stolzite $PbWO_4$ [2]

1.2.1 Photoelectric Effect

The photoelectric effect is the ejection of an electron from a material caused by the absorption of a photon. The ejected electron is called a photoelectron and has an energy of $E_e = \hbar\omega - E_B$, where E_B is the binding energy of electron and $\omega > E_B/\hbar$ is the angular frequency of the absorbed photon. In scintillators the binding energy is mostly regained by X-rays. A reasonable approximation for the cross section is

$$\sigma \propto \frac{Z^\nu}{E_\gamma^3} \tag{1.6}$$

where ν varies between 4 and 5 depending on the energy. The cross section has a strong dependency on the atomic number Z, which corresponds to the number of protons of the material. Also, the cross section rapidly decreases with energy above the typical electron binding energies, which makes it dominant for small energies. Therefore, the photopeak is typically not seen in our scintillation spectra for gammas of few hundred keV or several MeV energy.

1.2.2 Compton effect

Compton scattering is the interaction of a photon and an electron, called compton-electron. The photon has an energy of E_γ with a corresponding wavelength of λ, which leads to a reduced energy E'_γ after the scattering with the electron at an angle of θ. The conservation of energy and momentum leads to the following equation:

$$E'_\gamma = \frac{E_\gamma}{1 + \frac{E_\gamma}{m_e c^2}(1 - \cos\theta)} \tag{1.7}$$

$$\rightarrow \Delta E = E_\gamma - E'_\gamma = E_\gamma \left(1 - \frac{1}{1 + \frac{E_\gamma}{m_e c^2}(1 - \cos\theta)}\right) \tag{1.8}$$

The cross section for $E_\gamma \ll m_e c^2$ is the so-called Thomson limit

$$\sigma_T \simeq \frac{8\pi r_e^2}{3} \tag{1.9}$$

where $r_e = \frac{e^2}{4\pi\epsilon_0 m_e c^2}$ is the classical radius of an electron with the vacuum permittivity ϵ_0.

For large photon energy $E_\gamma \gg m_e c^2$ we are in the Klein–Nishina regime and the cross section follows

$$\sigma_{KN} \simeq \frac{3\sigma_T}{8} \frac{\ln 2E_\gamma}{E_\gamma} \tag{1.10}$$

which leads to a fall off with increasing energy. Compton scattering is the most relevant interaction for the measurements discussed in this thesis.

1.2.3 Pair creation

Pair creation is the most important interaction for a photon with large energy of a few tens of MeV. A high-energy photon has a non-negligible probability of transforming itself into a negative and a positive electron if an external field e.g. of a nucleus is present, and if it is not it's kinematically forbidden. Due to energy conservation, the energy of the electron E_{e^-} and of the positron E_{e^+} have to add up to the energy of the primary photon E_γ.

$$E_\gamma = E_{e^+} + E_{e^-} \tag{1.11}$$

The cross section reaches its asymptotic value at a few 100 MeV.

$$\sigma \simeq \frac{7}{9}\frac{1}{n_a X_0} \tag{1.12}$$

where n_a is the density of atomic nuclei per unit volume and X_0 is the radiation length in which the energy is reduced to a fraction of $1/e$.

1.3 Neutrons

Due to the fact that a neutron carries no electric charge, it interacts with the nucleus of an atom. The interaction can be divided into two major categories [4]: scattering and absorption (Figure 1.3).

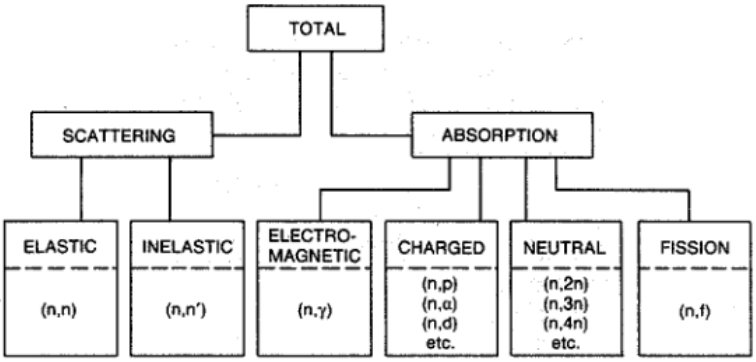

Figure 1.3: Various categories of neutron interactions. The letters separated by commas in the parentheses show the incoming and outgoing particles [4].

Scattering events can be elastic or inelastic. For elastic scattering, the total kinetic energy of the neutron and nucleus is unchanged. During this interaction a fraction of the neutrons kinetic energy is transferred to the nucleus, where the average energy loss per collision is $2E_nA/(A+1)^2$ with E_n the kinetic energy of the neutron and the mass number A of the nucleus. Inelastic scattering is similar to elastic scattering except that the nucleus gets into an excited state through internal rearrangement,

which eventually leads to a release of radiation. Therefore, the total kinetic energy of neutron and nucleus is not conserved.

Also, possible is the absorption or capture of a neutron by a nucleus. An emission may follow this process, which can be gammas, charged particles commonly protons, deuterons and alpha particles. Also, possible is the emission of one or more neutrons, which in the first case is indistinguishable from a scattering event. Furthermore, there may be a fission event, leading to two or more fission fragments and neutrons (the symbol is a "f" in Figure 1.3).

In our organic liquid scintillators, the neutron interacts with the nuclei of the molecules via scattering. The involved protons have a higher energy loss per unit length than electrons of the same energy. The higher ionisation density along the particle track is responsible for a loss in scintillation efficiency due to the fact that the production of detectable light is hindered by various processes, e.g. more internal conversions [3]. Therefore, the measured deposited energy in a scintillator is called visible energy (eV_{vis}). After thermalization most neutrons are captured in typical organic scintillator detectors on hydrogen nuclei. This process is followed by the emission of a 2.2 MeV gamma. To obtain more characteristic signatures, the scintillator can be loaded with metals having higher cross-sections for thermal neutron capture as gadolinium, lithium, boron or cadmium.

1.4 Fluorescence

Fluorescence is the emission of light by a substance after initial excitation, e.g. by photons. In an organic liquid scintillator the excitation of the aromatic solvent molecules mainly happens for delocalized electrons in the π-bonds of the sp^2 hybridized phenyl groups. Excitation of electrons in the σ-bonds on the other hand leads to the transformation to thermal energy. The emitted light is in most cases wavelength-shifted due to the Stokes-shift. A molecule with N atoms has 3N degrees of freedom consisting of translation, rotation and vibration degrees of freedom. If a molecule gets excited by the absorption of a photon, there are different processes that can happen to get back to the ground state. For example, collision processes with other molecules that transforms the energy into thermal energy. Also, redistribution of the energy between the different degrees of freedom, which is called internal conversion, play a role especially for large molecules. When two electronic states of the same molecule are close enough together, it is possible that the electronic state is lowered by transferring energy radiationless to vibrational modes of the molecule, which is then transformed into thermal energy. The energy gap between the ground state S_0 and the first excited state S_1 is normally larger than the gap of S_1 and S_2, which makes internal conversion unlikely [5]. Here the electron looses its energy by a spontaneous emission of a photon but with a larger wavelength than the absorbed one (Figure 1.4).

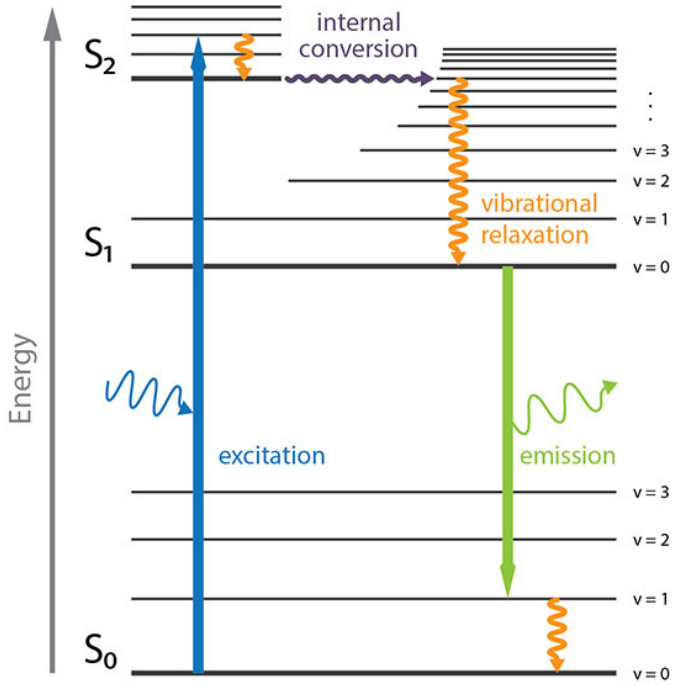

Figure 1.4: Simplified diagram for fluorescence [6]

2 Energy transfer mechanisms in organic scintillators

The energy transfer in an organic liquid scintillator determines the efficiency of the transformation of deposited energy to detectable photons. The light yield is defined as the amount of detectable photons per deposited energy, which is correlated to the energy resolution of the scintillator, and is approximately proportional to the deposited energy.

2.1 Scintillator composition

Liquid scintillators consist of one or multiple solvents, a primary fluor and if necessary a secondary fluor. Commonly used solvents are for example LAB, p-Xylol and Pseudocumol (Figure 2.1, 2.2 & 2.3).

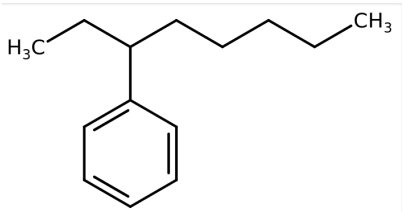

Figure 2.1: LAB (Linear alkylbenezene) [C1]

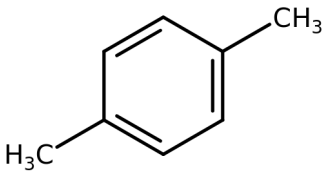

Figure 2.2: p-Xylol(1,4-Dimethylbenzene) [C2]

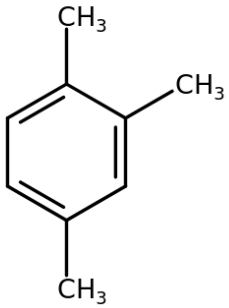

Figure 2.3: Pseudocumol(1,2,4-Trimethylbenzene) [C3]

Fluors play a crucial role for the scintillator because of the characteristic fluorescence. They are added only in small amounts, which makes a direct excitation less

important. Nevertheless, the fluors are very important for the energy transfer in the scintillator due to the excitation by solvents. They are used as wavelength-shifter to shift the emission spectrum of the scintillator to larger wavelengths, where the scintillator is more transparent for the light. The fluor has to be chosen, such that the absorption spectrum has a large overlap with the emission spectrum of the donor, which is the excited solvent molecule. This makes the probability of a transfer of the energy between donor and acceptor, the unexcited fluor molecule, high. In Figure 2.4 PPO is shown, which is often a good choice as primary fluor.

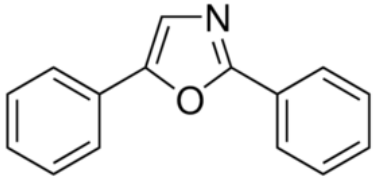

Figure 2.4: PPO (2,5-Diphenyloxazol) [C4]

A secondary fluor is needed if the wavelength of the emitted light of the primary fluor is not matching the wavelength region of the highest sensitivity for the photomultiplier cathode (section 5.2) or in large detectors when self-absorption of scintillation light becomes significant [7]. It can be excited by the primary fluor to shift the emission spectrum to even larger wavelengths. Therefore the secondary fluor has to be chosen with respect to the emission spectrum of the primary fluor. Commonly, POPOP (Figure 2.5) or Bis-MSB (Figure 2.6) are used in combination with PPO.

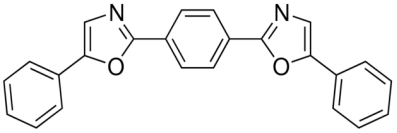

Figure 2.5: POPOP(1,4-Bis-(5-phenyl-2-oxazolyl)-benzol) [C5]

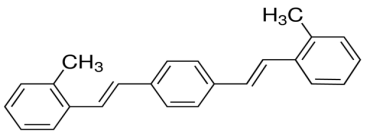

Figure 2.6: Bis-MSB(1,4-Bis-(2-methylstyryl)-benzol) [C6]

2.2 Energy transfer between single molecules

A simple model for the radiationless energy transfer between single molecules can be made with the assumption that energy transfer is independent of the distance between the donor and acceptor. Then the relative efficiency $\frac{\eta}{\eta_{max}}$ of the energy transfer can be described by [8]

$$\frac{\eta}{\eta_{max}} = \frac{1}{1 + \frac{c_0}{c}} \tag{2.1}$$

where c is the concentration of the acceptor molecule and c_0 is the critical concentration of the model. The equation 2.1 shows that the relative energy transfer is

depending on the concentration of the acceptor molecule.

In this model, the radiationless energy transfer is expected to be collisions between molecules. But there are more processes involved, and the most important one is the dipole-dipole-coupling (Förster resonance energy transfer, FRET). If the emission spectrum of a molecule overlaps with the absorption spectrum of another molecule, there is a possibility that the first molecule gets de-excited and the other one simultaneous excited. With the assumption that the energy is always transferred if the distance between donor and acceptor r is smaller than a critical distance R_0 and never if $r \leq R_0$ we get the model [9]:

$$\frac{\eta}{\eta_{max}} = 1 - e^{-\frac{c}{c_0}} \tag{2.2}$$

A quantum mechanical approach gives us a more complex but also more precise model:

$$\frac{\eta}{\eta_{max}} = \sqrt{\pi} x e^{x^2} (1 - \mathrm{Erf}(x)) \tag{2.3}$$

where $x = \frac{\sqrt{\pi}}{2} \frac{c}{c_0}$ and $\mathrm{Erf}(x) = \frac{2}{\sqrt{\pi}} \int_0^x e^{-u^2} du$ is the Gauss error function. The critical concentration can be described by the critical distance R_0 with $c_0 = \frac{3000}{4\pi N_A R_0^3}$ [10]. There are more processes like the dipole-quadrupole-interaction, but these processes have a very minor effect on the energy transfer and can be neglected.

High donor-concentration

The concentration of solvent molecules excited by ionizing particles in an organic liquid scintillator is very high due to the high concentration of the solvent itself. At a high concentration of excited solvent molecules, two effects play an important role: the diffusion of excited solvent molecules through the scintillator and the transfer of energy from solvent molecule to solvent molecule [11]. Both processes enable an energy transfer over large distances from a solvent molecule to fluor molecule.

A light-yield-model for a scintillator with two solvents, a quenching molecule and one fluor can be found in the appendix (Appendix A).

Part II

Experimental setup

The most crucial characteristics of a liquid scintillator are the transparency, light yield and Pulse Shape Discrimination. The transparency of light at a certain wavelength is important due to self-absorption. If the self-absorption of a liquid scintillator is too high, the light will not reach the photomultiplier tube and therefore can not be detected. Therefore, we measure the attenuation length of each sample of interest with a UV/Vis-spectrometer (chapter 3).

Moreover, we want to measure the light yield and Pulse Shape Discrimination capability. The higher the light yield, the higher the energy resolution of a sample. Different ionising particles can be distinguished via Pulse Shape Discrimination, which can be used e.g. to filter out interfering signals. For the measurements we need radioactive sources (chapter 4), a scintillator module (chapter 5) which consists of the liquid scintillator and a photomultiplier, and a data acquisition system (chapter 6). The measurement procedure is described in chapter 7.

The data file produced by the DAQ has to be analysed. The analysis methods are described in chapter 8 and 9. The analysis is based on C++ in combination with ROOT. It uses self written macros, which are analysing the light yield and Pulse Shape Discrimiation almost completely automatically (chapter 10).

3 UV/Vis Spectroscopy

With the UV/Vis-spectrometer at the MPIK we can measure the absorption spectra of solvents, scintillators or fluors that are dissolved in cylohexane, which is transparent above 210 nm. The UV/Vis-spectrometer measures the attenuation of the intensity of a light beam at a certain wavelength, which has to pass a sample cell with a typical pathlength of 1 or 10 cm, depending on the expected intensity, compared to a light beam, which traverse through air. Possible wavelengths of the light source are 175 nm (UV) to 900 nm (infrared) with a step size of 1 nm. The attenuation of the intensity I of the light traversing a sample of the thickness x is [7] :

$$I(x) = I(0)e^{-x/\Lambda} \tag{3.1}$$

with the attenuation length Λ of the sample. The absorption A is defined as $A = \log_{10}\left(\frac{I(0)}{I(x)}\right)$ and therefore the attenuation length can be calculated with:

$$\Lambda = \log_{10}(e)\frac{x}{A} \approx 0.4343\frac{x}{A} \tag{3.2}$$

Due to the fact that the light traversing the sample crosses four material transitions (air-glass, glass-sample, sample-glass, glass-air), which the reference beam $I(0)$ does not, we have to correct for the corresponding reflections. Due to the fact that the refractive index is wavelength dependent (dispersion) we have to correct the absorption $A(\lambda)$ of each wavelength. After the reflection and offset correction one gets an absorption spectrum as in Figure 3.1. The attenuation length of each solvent (Part IV) before and after column purification, except for S-04V, was measured.

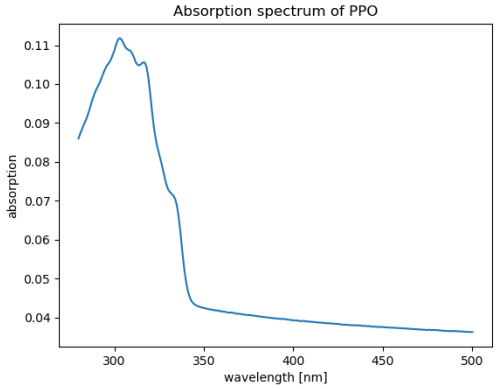

Figure 3.1: Absorption spectrum of PPO measured with the UV/Vis-spectrometer at the MPIK. The recorded wavelength region is 280 nm - 500 nm. Data provided by Benjamin Gramlich.

4 Radioactive sources

We use two different radioactive sources to measure the light yield and the PSD. The light yield measurements are performed with a Caesium-137 source and the PSD measurements with an AmBe neutron source.

4.1 Caesium-137

Caesium-137 (^{137}Cs) has a half-life of 30.17 years [13] and decays via beta decay either into stable Barium-137 (^{137}Ba) or into a meta-stable form of barium ^{137m}Ba. The meta-stable isotope rapidly converts into the stable ^{137}Ba , with a half-life of about 2 minutes, by the emission of a photon with an energy of 0.662 MeV [14].

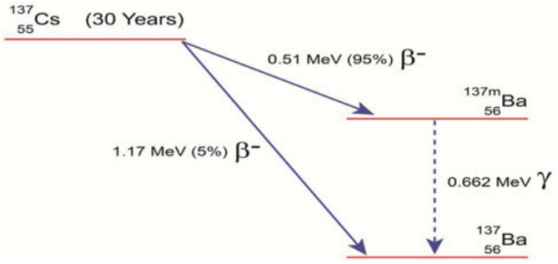

Figure 4.1: Decay scheme of ^{137}Cs [14]

As shown in Figure 4.1 the first beta decay mode that forms ^{137m}Ba accounts for approximately 95% of the total intensity and the second decay mode accounts for about 5%. The activity of the ^{137}Cs source used in our measurements is 130.98 kBq (2021). The reasons we use this source for the light yield measurements are that we get a very clean Compton-spectrum due to single gamma emission of ^{137}Cs, which is important to determine the light yield. Due to relative low energies of the Compton–electrons we get no saturation effects in the DAQ system. Figure 4.2 shows the energy spectrum of ^{137}Cs (the scintillator is LAB with PPO and POPOP as fluors). The peak at around 75 ADC are probably X-rays from K_α emission of ^{137}Ba [15] and the peak around 850 ADC is the compton-edge. The photopeak is missing due to the low atomic number of the scintillator and the strong dependency of the related photoelectric effect (subsection 1.2.1).

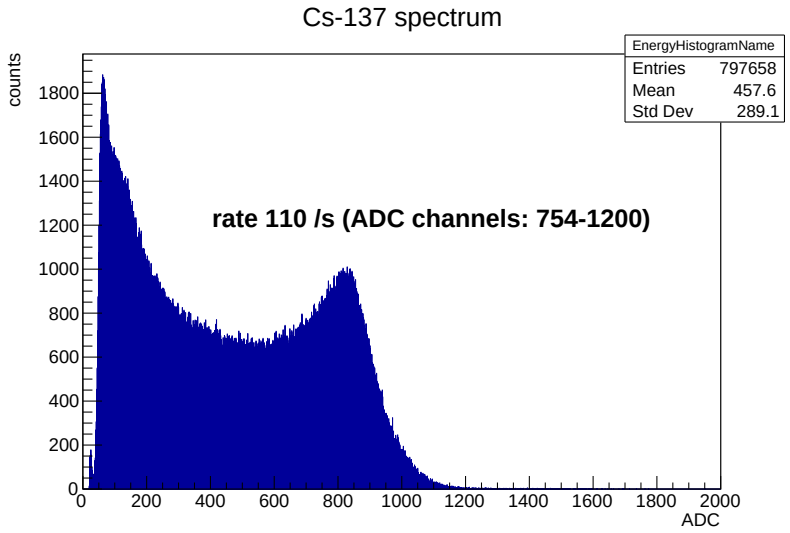

Figure 4.2: Compton spectrum of ^{137}Cs with LAB (PPO,POPOP) as a scintillator including the detected rate around the Compton-edge.

4.2 Americium-Beryllium

For the Pulse Shape Discrimination (PSD) measurement, we need a radioactive source with two different types of ionising radiation. Therefore, we use an Americium-Beryllium (AmBe) neutron source. Americium (^{241}Am) is radioactive and has a half-life of 432.2 years. It decays into Neptunium-237 (^{237}Np), which has a half-life of over 2 million years [16], via α-emission with five different energies averaging at about 5.5 MeV:

$$^{241}\mathrm{Am} \rightarrow {}^{237}\mathrm{Np} + \alpha + \gamma \tag{4.1}$$

where the energy of the photon is $E_\gamma \leq 1015$ keV. The α particles from the decay can produce neutrons when interacting with the stable Beryllium (^9Be).

$$\alpha + {}^{9}\mathrm{Be} \rightarrow {}^{13}\mathrm{C}^* \tag{4.2}$$

Depending on the interaction and the kinematics, Carbon-12 (^{12}C) and a free neutron may be produced. The two decay channels with the highest probability for the ^{12}C electromagnetic transition are [17]:

$$^{13}\mathrm{C}^* \rightarrow {}^{12}\mathrm{C} + n \tag{4.3}$$

$$^{13}\mathrm{C}^* \rightarrow {}^{12}\mathrm{C} + n + \gamma_1 \tag{4.4}$$

where $^{13}C^*$ is the excited ^{13}C molecule and γ_1 has an energy of $E_{\gamma_1} = 4.438$ MeV. The energy of the free neutron has its maximum value at about 11 MeV. If the energies get too high, the CAEN DAQ gets saturated and these events get rejected.

Since the PSD capability is reaching a plateau above ~ 1 $\mathrm{MeV_{vis}}$, higher energies are not relevant for the analysis. The activity of the AmBe source is 1.1 GBq and produces about $70 \cdot 10^3$ neutrons/sec. The source produces alphas, photons and neutrons.

$$\mathrm{AmBe} \Rightarrow \alpha + \gamma + n \tag{4.5}$$

Due to the very short interaction length of the alphas they are not able to reach the liquid scintillator and are therefore not relevant for the measurement.

4.3 Background radiation

Due to cosmic radiation and natural radioactivity, we also detect background radiation. The background energy spectrum is shown in Figure 4.3. Compared to the energy spectrum of ^{137}Cs (Figure 4.2) the intensity of the background radiation is very low, especially in the region of the compton-edge (about 2% of the Cs-137 source), and therefore a correction for the background is not performed.

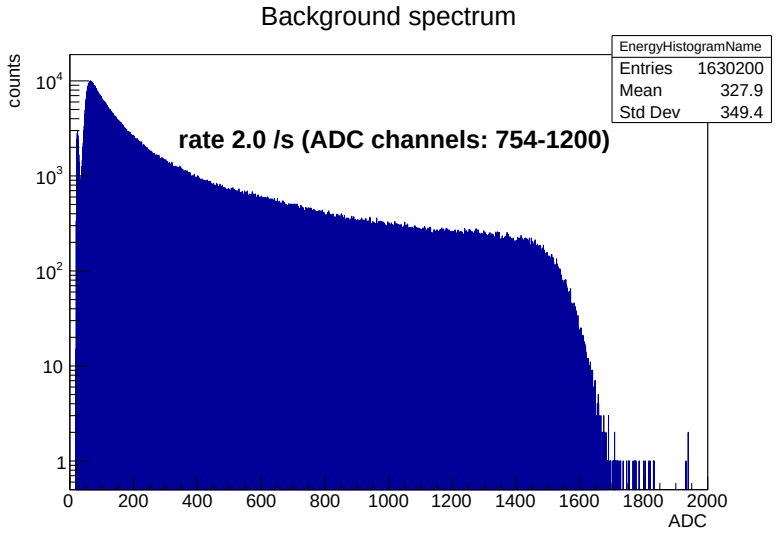

Figure 4.3: Background radiation measured with a LAB (PPO,POPOP) scintillator for 24h.

5 Scintillator module

The scintillator module (Figure 5.1) consists of a liquid container, the photomultiplier tube (PMT) and the plugs for the high voltage and the signal.

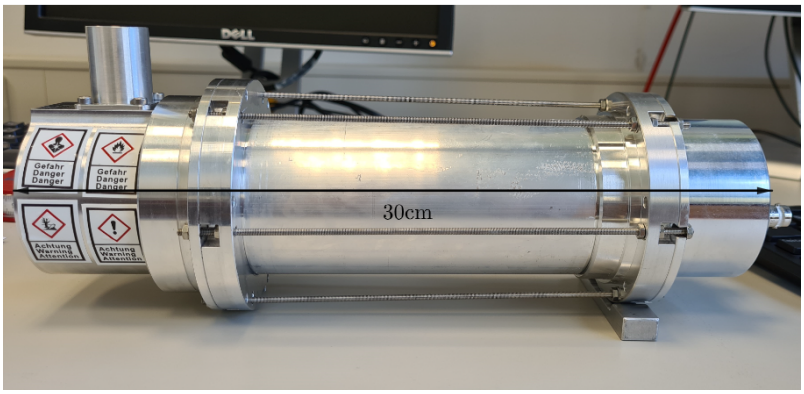

Figure 5.1: Scintillator module

The scintillator module was originally designed and constructed at MPIK in the context of a Ge-quenching measurement campaign. It was acting as a coincidence detector to identify neutrons which scattered on a Ge crystal before. Now, the module was used for the first time in the context of the scintillator characterization activities at MPIK.

5.1 Liquid container

The liquid container is the container for the liquid scintillator and therefore has to be airtight and light-proof. It has a capacity of about 117 ml and an inner diameter of 6.5 cm (Figure 5.3). The liquid scintillator is separated from the PMT by a UV-transparent glass plate. The filling of the liquid container and the bubbling of the liquid scintillator is done via a chimney at the side of the cylindrical vessel (Figure 5.2). The vessel consists of a PTFE block, which guarantees a high reflectivity, contained in a housing made of aluminium-magnesium alloy.

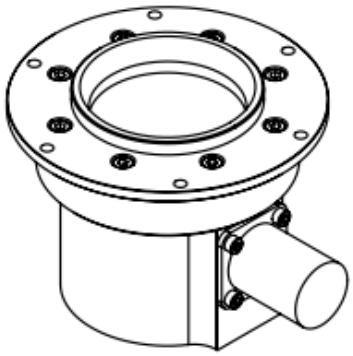

Figure 5.2: Design drawing of the liquid container

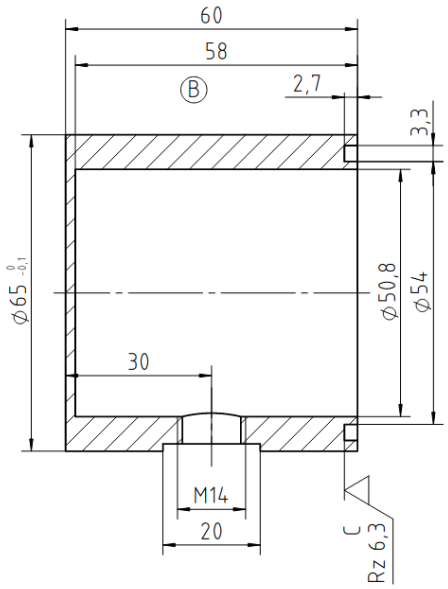

Figure 5.3: Cross-section of the liquid container (lengths in mm)

5.2 Photomultiplier tube

A photomultiplier tube (PMT) is a vacuum tube consisting of a photocathode, focusing electrodes, dynodes and an anode (Figure 5.4) [18].

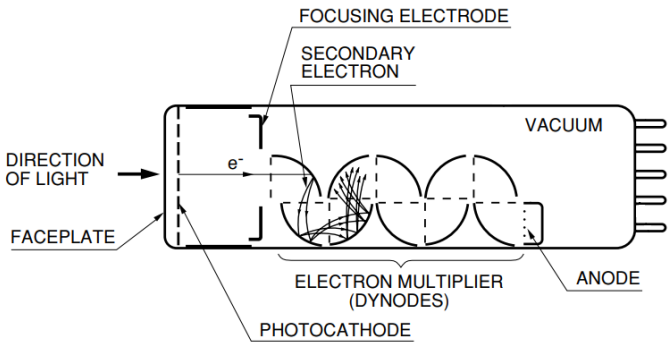

Figure 5.4: Construction of a PMT [18]

Light from the scintillator, which enters the PMT, will hit the photocathode and produce photoelectrons via the photoelectric effect. These photoelectrons are focused and accelerated by the focusing electrode onto the first dynode. The dynode is an electron multiplier due to the emission of secondary electrons. This emission is repeated at every single dynode, which leads to an exponential growth of the number of photoelectrons. Finally, the electrons are collected by the anode and produce a measurable signal. To get the electrons to hit the dynodes and the anode, one has to influence the electron movement by an electric field. For that, one has to apply a voltage between each dynode such that the electrons accelerate to the next dynode and finally to the anode. The high voltage (HV) used for the PMT is a NHQ203M module integrated in a NIM crate. The HV is set to 1.5 kV with positive polarity.

Quantum efficiency

When photons hit the photocathode electrons in the valence band become excited by the absorption of the photon energy. If the electrons have enough energy to overcome the vacuum barrier, they are emitted into the vacuum as photoelectrons. The probability of the whole process can be expressed as the quantum efficiency $\eta(\nu)$, which is the ratio of output electrons to the incident photons.

$$\eta(\nu) = (1 - R)\frac{P_\nu}{k}\frac{P_s}{1 + 1/(kL)} \tag{5.1}$$

where R is the reflection coefficient, k the full absorption coefficient of photons, P_ν the probability that light absorption may excite electrons to a level greater than the vacuum level, P_s the probability that electrons reaching the photocathode surface may be released into the vacuum, L the mean escape length of excited electrons and ν the frequency of light. Therefore, the frequency of the light has to be chosen such that the quantum efficiency is maximized. The PMT ETL9954B used for the scintillator module has a maximum quantum efficiency of about 27% at a wavelength of 400 nm [19].

Gain and current amplification

The collection efficiency α is the probability that photoelectrons will hit on the effective area of the first dynode. The effective area is the area where photoelectrons can be multiplied effectively without deviating from their favourable trajectories to hit the successive dynodes. Secondary electrons at later dynodes will have less of an effect on the total collection efficiency due to the exponentially increasing number of secondary electrons.

The secondary emission ratio at each dynode is given as a function of interstage voltage E:

$$\delta = aE^k = a\left(\frac{V}{n+1}\right)^k \tag{5.2}$$

where a is a constant, k is determined by the structure and material of the dynode, V is the supply voltage and n is the number of dynode stages.

The current amplification μ, also called gain, is then given by:

$$\mu = \alpha \cdot \delta^n = \alpha \cdot AV^{kn} \tag{5.3}$$

where $A = a^n/(n+1)^{kn}$ is a constant.

Scintillation counting

In order to make scintillation counting possible, our scintillator in the liquid container is attached to the PMT with optical grease having a similar refractive index as glass to minimize light losses due to reflections at the surfaces of the material transitions (Figure 5.5).

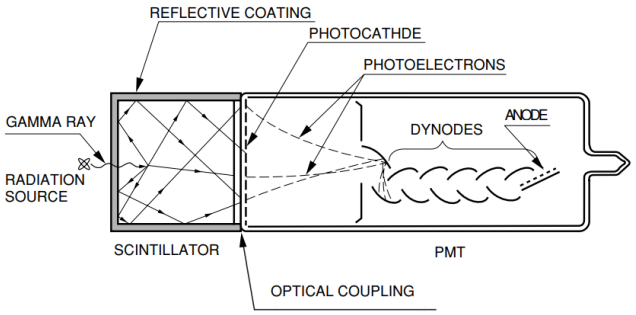

Figure 5.5: Scintillator and PMT [18]

The energy resolution of this setup is a combination of the energy resolution of the scintillator R_s and the energy resolution of the PMT R_p:

$$R(E)^2 = R_s(E)^2 + R_p(E)^2 \tag{5.4}$$

The energy resolution of the PMT depends mainly on the quantum efficiency η and the collection efficiency α. The total energy resolution mainly depends on the statistical error $\propto \frac{1}{\sqrt{n}}$ where n is the number of photoelectrons.

Also important is the linearity of the output signal of the PMT with respect to the amount of light of the scintillator. The PMT itself has a very good linearity over the relevant range of incident light levels.

In Figure 5.6 shows the average pulse of a LAB based scintillator for a neutron and gamma.

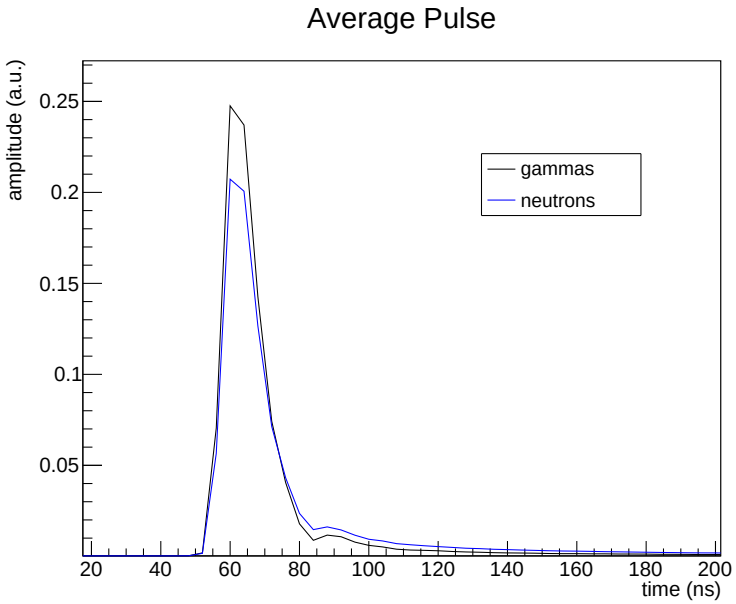

Figure 5.6: Average pulse of a LAB based scintillator. The amplitude is given as absolute difference between pulse and baseline in arbitrary units (a.u.). In blue the average neutron pulse and in black the average gamma pulse. The kink at about 85 ns is an artifact probably caused by the electronic components in the PMT base. We do not expect significant impact on the results of our relative measurements, since the effect is similar in all samples. The difference in the pulse shape of the neutron and gamma events are described in chapter 9.

The pulse $f(t)$ can be modeled by a sum of exponentials [20]:

$$f(t) = \sum_i \frac{q_i}{\tau_i} e^{-\frac{t}{\tau_i}} \tag{5.5}$$

where τ_i is the decay time and q_i the weight of the i-th term. The components can be separated into fast and slow components. The decay times are normally very fast e.g. gammas in LAB about $\tau_1 = 6$ ns for the fast components and $\tau_2 = 96$ ns and $\tau_3 = 79$ ns for the slow components [20]. The fast component provides the dominant

contribution to the pulse. It is related to the de-excitation of the lowest excited singlet spin-state S_1 in the solute. The other components arise from processes such as the de-excitation of electrons in the triplet spin-states [21]. The pulse saturates in the DAQ module, if the pulse height is larger than 2 V (see dynamic range in subsection 6.2.1).

6 DAQ (CAEN system)

The data acquisition system (DAQ) used for our measurements is a CAEN system, which consists of a CAEN module and the CoMPASS software [22] [23]. The CAEN module was tested in the context of the CONUS experiment [24] and is used here for the first time for the scintillator characterization at MPIK.

6.1 Hardware Setup

The experimental setup consists of a radioactive source, the scintillator module, a high voltage power supply, a CAEN module and a PC with the CoMPASS software (Figure 6.1).

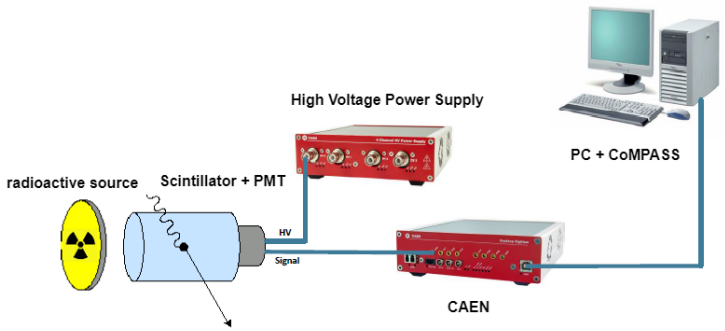

Figure 6.1: Hardware setup [23]

The CAEN VME module V1725S [25] used has 16 slots for scintillator signals (16 channel), 14 bit which corresponds to 16384 bins, although we set them to 4096, and a sampling rate of 250 MS/s, which gives us one sample every 4 nanoseconds (ns). The CAEN module gets the signal from the scintillator as an analog signal and has to convert it into a digital signal (analog-to-digital converter). The communication from and to the board is provided by a VMEBus and optical link interfaces. The module V1725S can not only record the charge of each pulse but is also capable of recording the waveforms (Figure 6.2).

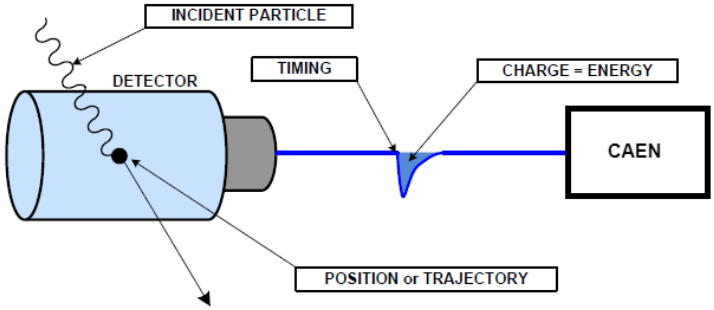

Figure 6.2: Signal of the scintillator module [23]

The analog signal is a continuous signal with continuous values, while the digital signal is a sequence of discrete values (Figure 6.3).

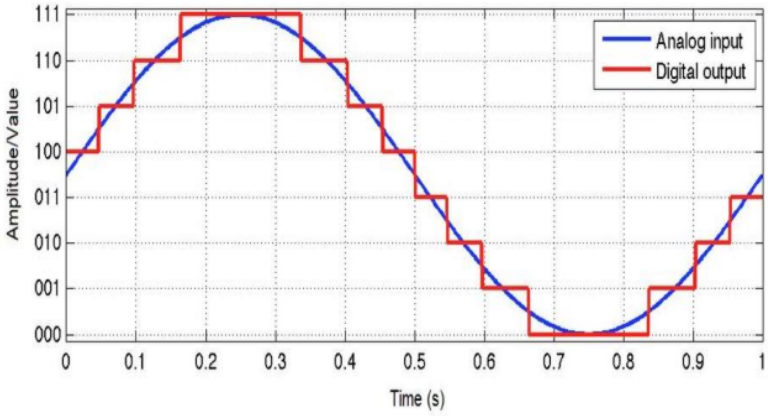

Figure 6.3: Analog to digital conversion [26]

Nowadays, the Analog to Digital conversion occurs as close as possible to the detector to minimize the information loss. The acquisition of the digital signal will be affected by uncertainties due to the quantization noise, which depends on the sampling rate and the number of possible bins (ADC-channels), and to other sources of electronic noise.

But the CAEN is not just an analog to digital converter, it has many more features, which are controlled by the CoMPASS software.

6.2 CoMPASS software

6.2.1 Input

For the input signal one has to set the record length in ns for each pulse, the pre trigger which defines the amount of time in ns before the trigger in the waveform which is saved into the memory, the polarity of the pulse, the amount of samples for the baseline (bl.s.) with its fixed value (bl.v.) and the DC offset in %, which adjusts the baseline position such that there is no DC offset in the recorded data. Also, the input dynamic, which is the possible difference between the maximum and the minimum of a signal [27], can be set to $0.5V_{pp}$ or $2V_{pp}$, where V_{pp} is the peak-to-peak value. Table 6.1 shows our input settings.

Record length	Pre trigger	polarity	bl. s./v.	DC offset	input dynamic
992 ns	96 ns	negative	256/0	20%	$2.0V_{pp}$

Table 6.1: Input settings used for measurements

6.2.2 Discriminator

A discriminator produces a logical output pulse when the pulse height of an input signal is above a certain threshold or if it is above a certain constant fraction, depending on the discriminator mode used. There are two possible discriminator modes that can be selected in the CoMPASS software: leading edge or CFD. The leading edge (LE) mode uses a threshold in units of lsb (least significant bit) that has to be reached for a recorded input signal. This mode is used for the light yield measurements to filter out most of the background noise (Table 6.2). The CFD (Constant Fraction Discriminator) mode uses a constant fraction of the signal that has to be reached. It is used for analog signals of varying heights but with the same rise time. It is done by splitting the input signal, attenuating one of it and delaying the other one. Then the delayed signal is inverted and both are added together, which results in a constant fraction trigger when the value of the signal crosses the zero line [28]. The Constant Fraction Discriminator is used for our PSD measurements to have a comparable start time for all recorded signals. To prohibit that the trigger triggers multiple times for the same signal, we have to set a trigger holdoff with a value larger than the record time of the signal.

Threshold LE/ Threshold CFD	Trigger holdoff	CFD fraction	CFD delay
500 lsb / 200 lsb	1024 ns	75 %	4 ns

Table 6.2: Discriminator settings used for measurements

6.2.3 Charge to Digital Converter (QDC)

To extract the charge/energy out of a recorded signal, we have to set a pre gate and a gate with a certain length, which is used to determine the charge/energy of a given signal by integrating from the end of the pre gate to the end of the gate (Figure 6.4). For the PSD measurements (chapter 9) one also need another gate called short gate, which is used to determine the charge/energy of the tail of the signal by the subtraction of the short gate energy E_{short} of the total energy E_{tot}. The short gate also starts directly after the pre gate.

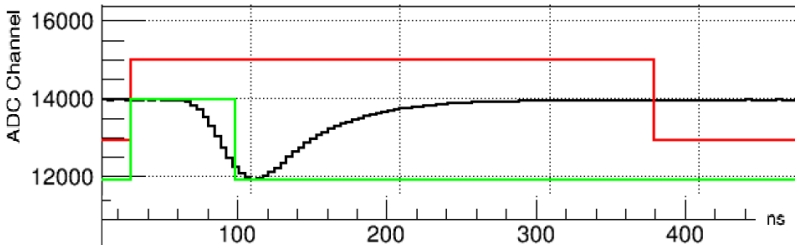

Figure 6.4: Pulse with different gates: short gate (green), gate (red) and pre gate (offset at the start) [23].

To optimize the dynamic range, one can adjust the energy coarse gain, which amplifies the original signal by a factor such that more of the ADC channels can be used but without getting events pushed into the saturation channel. Our QDC settings are shown in Table 6.3.

Energy coarse gain	Gate	Short gate	Pre gate
10 fC(LSB$\times V_{pp}$)	200 ns	40 ns	16 ns

Table 6.3: QDC settings used for measurements

6.2.4 Rejection and Spectra

Besides the rejection of saturation and pileup events, CoMPASS allows to set energy, PSD and time cuts while recording. Only the rejections are used in the measurement, the cuts are done offline, if needed, after the measurement. One can also the set the amount of energy, PSD and time channels used for the spectra (Table 6.4).

Energy channels	PSD channels	Time channels
4096	4096	8192

Table 6.4: Spectra settings used for measurements

Part III

Methods

7 Measurement procedure

7.1 Sample preparation

First of all the sample of interest has to be prepared. Therefore, we use a scale and tare it to the empty vessel used for the sample. Then the desired mixture can be adjusted by measuring the weight of each component. To speed up the dissolution of the used fluors, the samples get stirred by a magnetic stirrer, normally over night (Figure 7.1). Therefore, we have to place magnetic stir bars of the right size into the sample depending on the size of the used vessel.

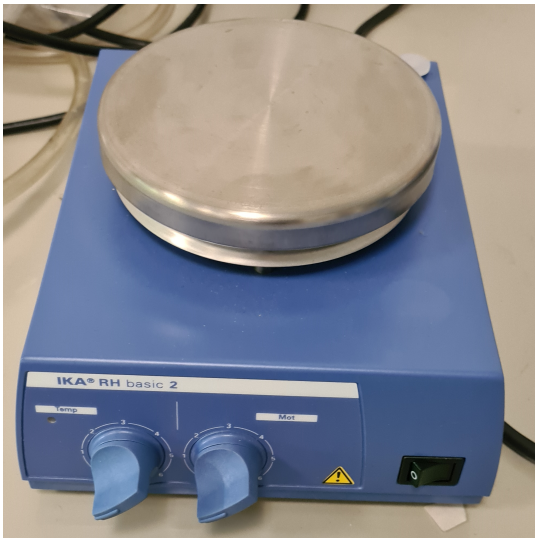

Figure 7.1: One of the magnetic stirrer at the MPIK. The left knob controls heating and the right the stirring rate.

7.2 Filling and bubbling

Once the fluors are dissolved, the sample gets filled into the liquid container of the scintillator module. Oxygen is a quenching molecule and therefore decreases the light yield up to about 20% [64]. Because of that we bubble the sample in the liquid container with argon or nitrogen for 10 minutes before measuring the light yield and PSD. Argon and nitrogen are chemically inert and do not quench the scintillation light. Moreover, there is no difference in light yield by bubbling with argon or nitrogen. This was tested by multiple measurements of the same scintillator sample but different bubbling method. The light yield measurement is done with a

^{137}Cs and the PSD measurement with a AmBe source. Each measurement takes 5 minutes.

7.3 Cleaning and disposal

After the light yield and PSD measurement the sample in the liquid container gets either disposed into a dedicated container or filled back into the mixing vessel. If it is filled back, the vessel will be bubbled with argon or nitrogen. After the removal of the sample the liquid container gets cleaned. Therefore, I flush it with isopropanol (C_3H_8O, Figure 7.2) or cyclohexane (C_6H_{12}, Figure 7.3). Cyclohexane can be easily removed by evaporation under the support of a gas flow. If the removed sample is the same mixture as the next one, but with slightly different concentrations, a cleaning of the cell is not needed. For the phenylsiloxanes we found that isopropanol is an excellent solvent to remove it from the liquid container.

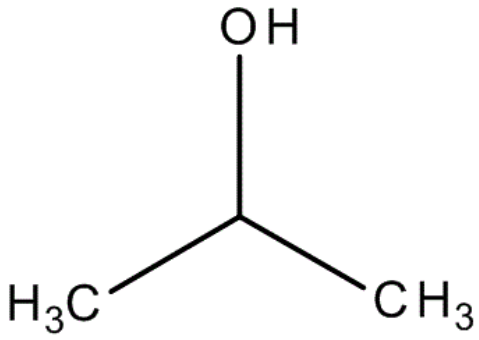

Figure 7.2: Isopropanol [C7]

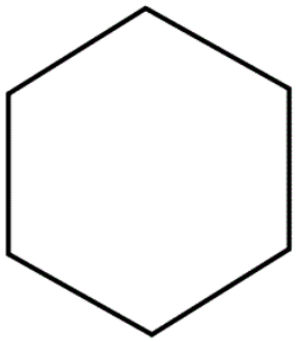

Figure 7.3: Cyclohexane [C8]

8 Light yield determination

The light yield is one of the most important quantities of a scintillator. It corresponds to the amount of photons per MeV of deposited energy in the scintillator. The higher the light yield, the better the energy resolution of a scintillator. To determine the light yield of a scintillator, one needs a reference point with known energy in the spectrum.

8.1 Compton spectrum

One way is to use the compton-edge of the compton spectrum, which is the energy value of a compton-scattering with an angle of 180° between photon and electron. The corresponding energy for ^{137}Cs can be calculated by Equation 1.8:

$$E_c = E\left(1 - \frac{1}{1 + \frac{E}{m_e c^2}(1 - \cos(\theta = 180°))}\right) \approx 478\text{keV} \tag{8.1}$$

where E is the photon energy of the radioactive source, which is $E = 0.662$ MeV in this case (section 4.1). Due to statistical errors like fluctuations in the amount of photons, photoelectrons and the baseline of a pulse, the compton-edge gets smeared out. To account for a finite energy resolution, we describe the errors by a Gaussian normal distribution:

$$G(E) = \frac{1}{\sqrt{2\pi\sigma^2}} \exp\left(-\frac{E^2}{2\sigma^2}\right) \tag{8.2}$$

where E is the energy and σ is the standard deviation. The recorded spectrum $R(E)$ emerges from the convolution of the ideal compton spectrum $r(E)$ and the Gaussian distribution [29]. The ideal compton spectrum can be described by:

$$r(E) = \begin{cases} aE^2 + bE + c & E \leq E_c \\ 0 & E > E_c \end{cases} \tag{8.3}$$

where a, b and c are parameters to describe a parabola.

$$\begin{aligned} R(E) = r(E) \otimes G(E) &= \int_{-\infty}^{\infty} r(x)G(E-x)dx \\ &= \alpha_1 \operatorname{Erfc}\left(\frac{E - E_c}{\sqrt{2}\sigma}\right) + \beta_1 \exp\left(-\frac{(E-E_c)^2}{2\sigma^2}\right) \end{aligned} \tag{8.4}$$

where $\mathrm{Erfc}(x) = 1 - \mathrm{Erf}(x)$, $\alpha_1 = \frac{1}{2}\left[a(E^2 + \sigma^2) + bE + c\right]$

and $\beta_1 = \frac{-\sigma}{\sqrt{2\pi}} a(E_c + E) + b$

To analyse the light yield of a scintillator, we can fit a certain range around the compton-edge in the energy spectrum with the function $R(E)$ and take the specific % value in the high energy tail of the peak. Literature values suggest values from 66% to 89% [29], but this optimum is detector and scintillator dependent. Then the corresponding energy value gives us the light yield in units of ADC. To study the impact and systematic uncertainty related to the choice of the reference point, I measured the energy spectrum of different scintillator samples and determined the light yield for different percentage values of the peak (Table 8.1).

Mixture	**rel. LY@50%**	**rel. LY@70%**	**rel. LY@80%**	**rel. LY@90%**
EJ301	1.000	1.000	1.000	1.000
ST-GC	0.682	0.661	0.673	0.671
ST-Target	0.525	0.508	0.516	0.512
DC-Target	0.503	0.485	0.494	0.490

Table 8.1: Light yield (LY) relative to EJ301 at different percentage values for the high energy tail of the peak. DC-Target is the liquid scintillator of the Double Chooz neutrino target, ST-Target and ST-GC are the liquid scintillator of STEREO for the target and gamma catcher respectively.

The measurements show that the deviation is rather small with about 2% difference between the relative light yield of the 70, 80 and 90% method. The light yield determined with the 50% value has a deviation nearly double as high. Therefore, the systematic error of the different percentage values between 70% and 90% is smaller than the total relative error of the light yield, which is $\frac{\Delta LY}{LY} = 0.024$. The total relative error of the light yield, which means the systematical and statistical error, was determined by multiple measurements of the light yield of the same scintillator with different fit ranges. The optimal percentage value was determined by a backscatter-peak measurement (section 8.2).

8.2 Backscatter-measurement

In the backscattering technique, we use the fact that the scattered photon can leave the scintillator cell and hit another scintillator detector. If we place the two scintillator cells such that they are exactly in line with each other and a radioactive source placed between them, then we can select events with a scattering angle of about 180° by a coincidence measurement. This means we only select events that happen within a certain time interval. Due to the finite volumes of the scintillator-cells, we do not get exactly 180° events, which means the energy is also not exactly

478 keV as calculated in Equation 8.1. This leads to an uncertainty in the light yield, which can be derived by the geometry of the setup. The uncertainty can be lowered by increasing the distance between the two scintillators, but that also decreases the amount of events detected, which would lead to a much longer detection-time to obtain the same statistics.

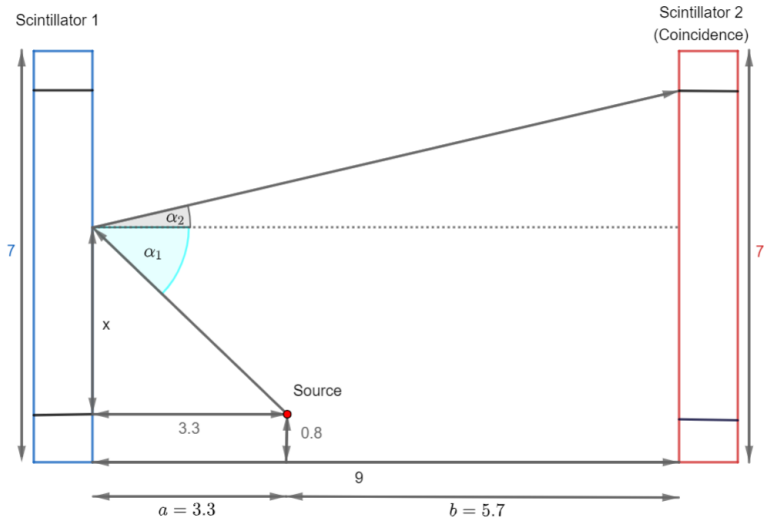

Figure 8.1: Setup of the coincidence measurement (all distances are in cm). The scintillator cells have an outer radius of 7 cm and an inner radius of 5.4 cm.

With Figure 8.1 we can determine the angle between the direction of the incoming photon and the direction of the outcoming compton-scattered photon:

$$\alpha(x) = \alpha_1(x) + \alpha_2(x) = \arctan\left(\frac{x}{3.3}\right) + \arctan\left(\frac{5.4 - x}{9}\right) \tag{8.5}$$

The maximum angle is at $x_{max} = 5.4$, which leads to an angle of $\alpha(x_{max}) = 58.57°$. So we get a maximum relative error of:

$$\Delta E_{rel} = \frac{E(180°) - E(180° - 58.57°)}{E(180°)} = 8.1\% \tag{8.6}$$

The fact that this method takes a couple of hours and the accuracy is not significantly improved, leads to our decision to only use the backscatter-method to determine the percentage value for the compton-edge peak used to determine the light yield. For all results presented in the following chapters the Compton method was applied.

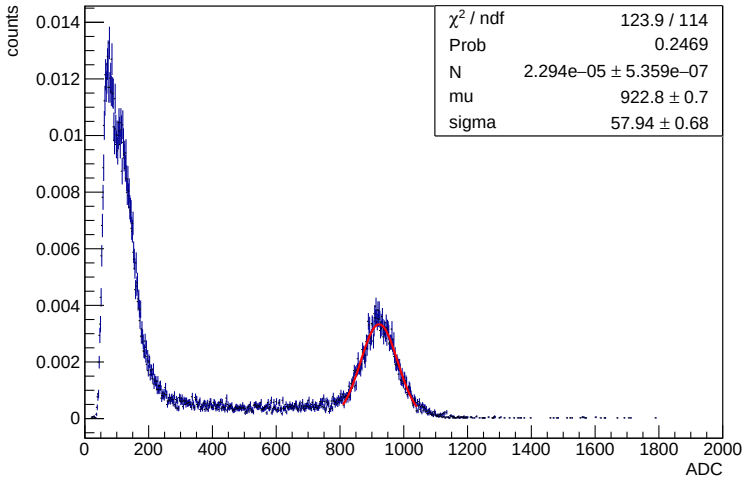

Figure 8.2: Backscatter peak

In Figure 8.2 the Compton backscattering peak is shown for a DIN (3 g/l PPO, 20 mg/l BisMSB) scintillator. The peak position at 923 ADC counts corresponds to a 70% value of the Compton-edge method with the identical liquid scintillator. Therefore we chose this 70% value as reference point for all measurements and results presented in the following chapters.

9 Pulse Shape Discrimination

Pulse shape discrimination (PSD) capability is one of the characteristic features of a scintillator. It describes the ability to distinguish between different particles of ionising radiation, e.g. α and β radiation. The de-excitation of the scintillator which follows an interaction depends on many different factors, but a special role plays the energy loss density. The larger the energy loss per unit of length dE/dx the larger is the slow component, which means the component that decays over long times, with respect to the fast component of a scintillator. The reason for that is the higher excitation ratio of triplet to singlet states and the fact that triplet states have a longer decay time. This dependence on dE/dx provides a tool to distinguish different particles [30] (Figure 9.1).

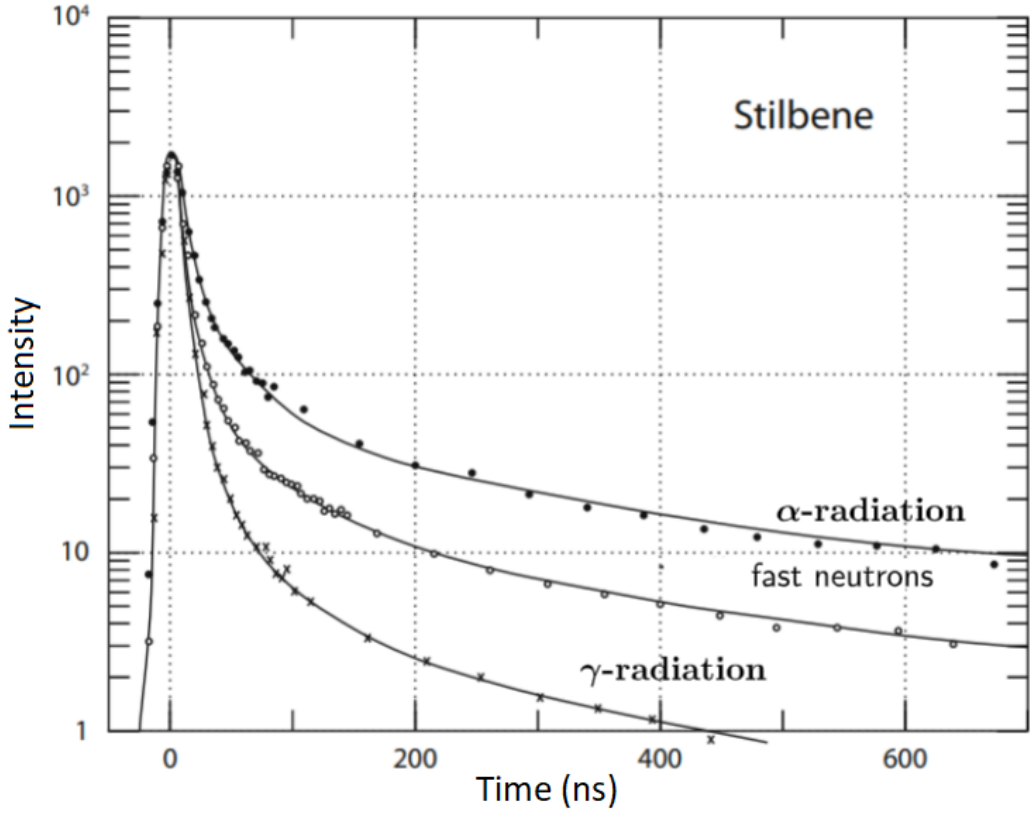

Figure 9.1: Pulse shape of gamma-radiation, fast neutrons and alpha-radiation in an organic scintillator (Stilbene) [1].

9.1 Tail-to-total method

The tail-to-total method relies on the integration of the signal over two different intervals, where one interval covers the whole signal and the other interval covers only the tail of the signal. The separation parameter is the ratio of the charge in the tail Q_{tail} to the charge in the whole signal Q_{tot} [30]:

$$\text{PSD} := \frac{Q_{tail}}{Q_{tot}} \tag{9.1}$$

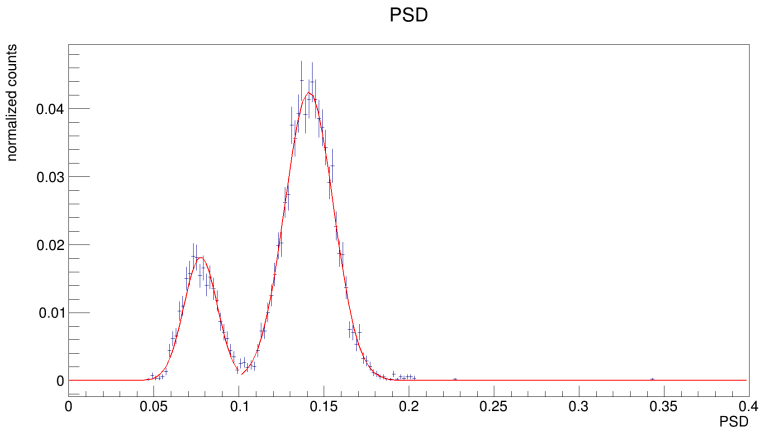

Figure 9.2: PSD of LAB(with PPO and POPOP) at the energy interval 1400-1500 ADC. The first peak is the electronic recoil and the second the nuclear recoil.

9.2 Figure of merit

The PSD parameter is different for different particle types and can be used to distinguish between those. To have a quantity to characterize the performance of a scintillator on separation power, we use two normal distribution for modelling the PSD of the nuclear and electronic recoil population for a given energy interval (Figure 9.2). Then we define the figure of merit (FoM) as [31]:

$$\text{FoM} := \frac{1}{2\sqrt{2\ln 2}} \frac{|\mu_n - \mu_e|}{\sigma_e + \sigma_n} \tag{9.2}$$

where μ_n and σ_n is the central value and the standard deviation of the nuclear recoil population and μ_e and σ_e is the same for the electronic recoil population. The quantity to describe the separation power FoM is energy dependent, but the asymptotic maximum can be used to compare different scintillators. The asymptotic maximum was determined by the fit-function (Figure 9.3):

$$y = \frac{a}{x} + b \tag{9.3}$$

with the free parameters a and b.

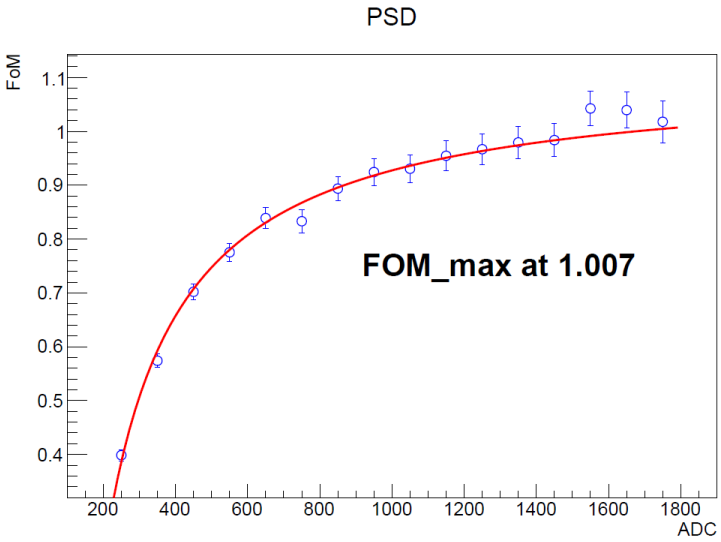

Figure 9.3: FoM of LAB (with PMP)

The relative error of the $\mathrm{FoM_{max}}$ was determined analogue to the error of the light yield. The relative error of the $\mathrm{FoM_{max}}$ value is $\frac{\Delta \mathrm{FoM_{max}}}{\mathrm{FoM_{max}}} = 0.01$.

10 Analysis code and file format

The CoMPASS software saves the data into histograms as a ROOT file. The file uses the so-called TTree class designed to store large quantities of same-class objects, which is optimized to reduce disk space and enhance access speed [32]. The TTree can be efficiently read out with the TTreeReader. Dr. Aurelie Bonhomme gave me the basic code frame to analyse the data based on a combination of C++ and ROOT. This code was extended to be able to analyse the light yield and PSD capability of a scintillator sample.

10.1 Code for light yield analysis

The code for the light yield was written, such that the light yield analysis is as automated as possible. It only needs the fit range and an estimation of the central value and thickness of the Compton-edge. It reads out the count and energy of each bin of histogram of the ROOT file, plots the energy spectrum as a histogram and fits Equation 8.4 in a selected region. The fit parameters and fit range can easily be determined by the fit panel of root, which enables interactive fitting for different fit ranges (Figure 10.1).

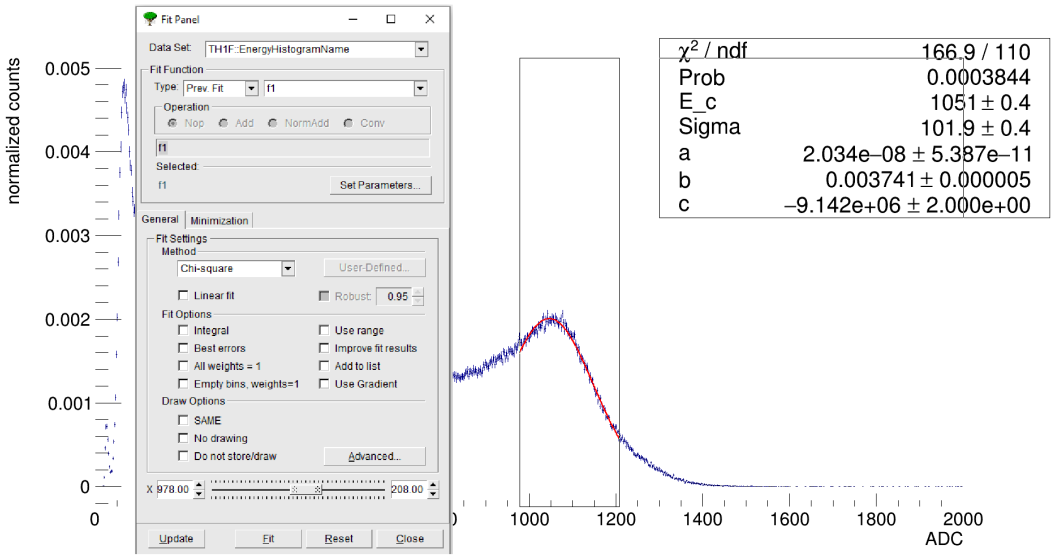

Figure 10.1: Example of the determination of the fit parameters with the fit panel. Left: Fit panel with selectable fit range. The box in the top right gives the values for the fit parameters. One has to vary the fit range, such that it has the best agreement with the Compton-edge.

After the selection of the fit range and fit parameters the light yield will be determined with the 70% value of the high energy tail of the Compton-edge (Figure 10.2). The energy histogram with the Compton-edge fit can be saved as a PDF file.

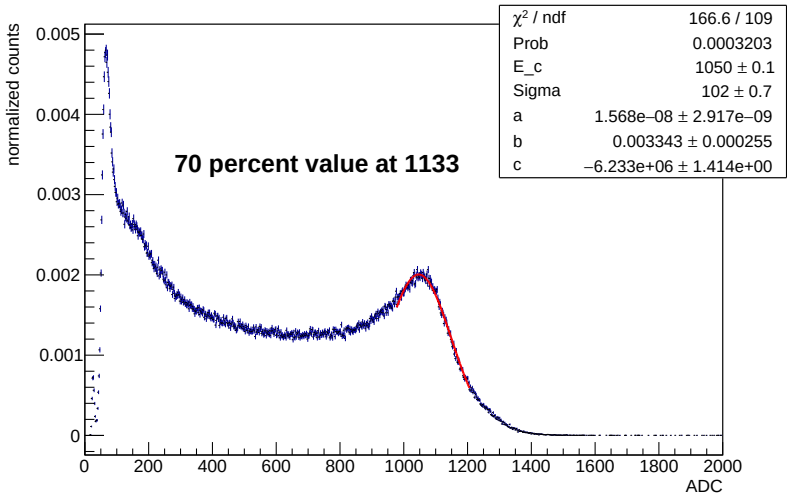

Figure 10.2: Determined light yield of a sample of EJ301.

10.2 Code for PSD analysis

For the PSD analysis one has to select two fit ranges, one for the nuclear and one for electronic recoil peak. For each peak one has to estimate the central value and the standard deviation. The written macro reads out the energy within each gate (subsection 6.2.3) for an energy interval of 100 ADC and calculates the PSD value (Equation 9.1). It then performs two fits one for the nuclear and one for the electronic recoil peak in each energy interval and then calculates the figure of merit (Equation 9.2) with the determined fit parameters. The fit ranges and parameters can be found with the selection of standard values, which produces the plot in Figure 10.3. One can see that in some energy intervals the nuclear and electronic recoil can not be distinguish either because they are too close together or because one of the peaks is missing. Therefore, some energy intervals have to be excluded in the calculation of the figure of merit. After selecting the right fit ranges, fit parameter and the energy intervals the FoM is plotted against energy and Equation 9.3 is fitted to determine the asymptotic maximum. The final result of this procedure was already previously shown in Figure 9.3, which can also be saved as a PDF file. If the fit has a bad agreement with the data, which leads to an over or underestimation of the asymptotic maximum, it might help to exclude some low energy data points e.g. start the fit at 500 ADC. This can happen due to the fact that for low energies the pulses of the different ionisation particles are more difficult to distinguish, which leads to a larger uncertainty in the figure of merit as compared to higher energies.

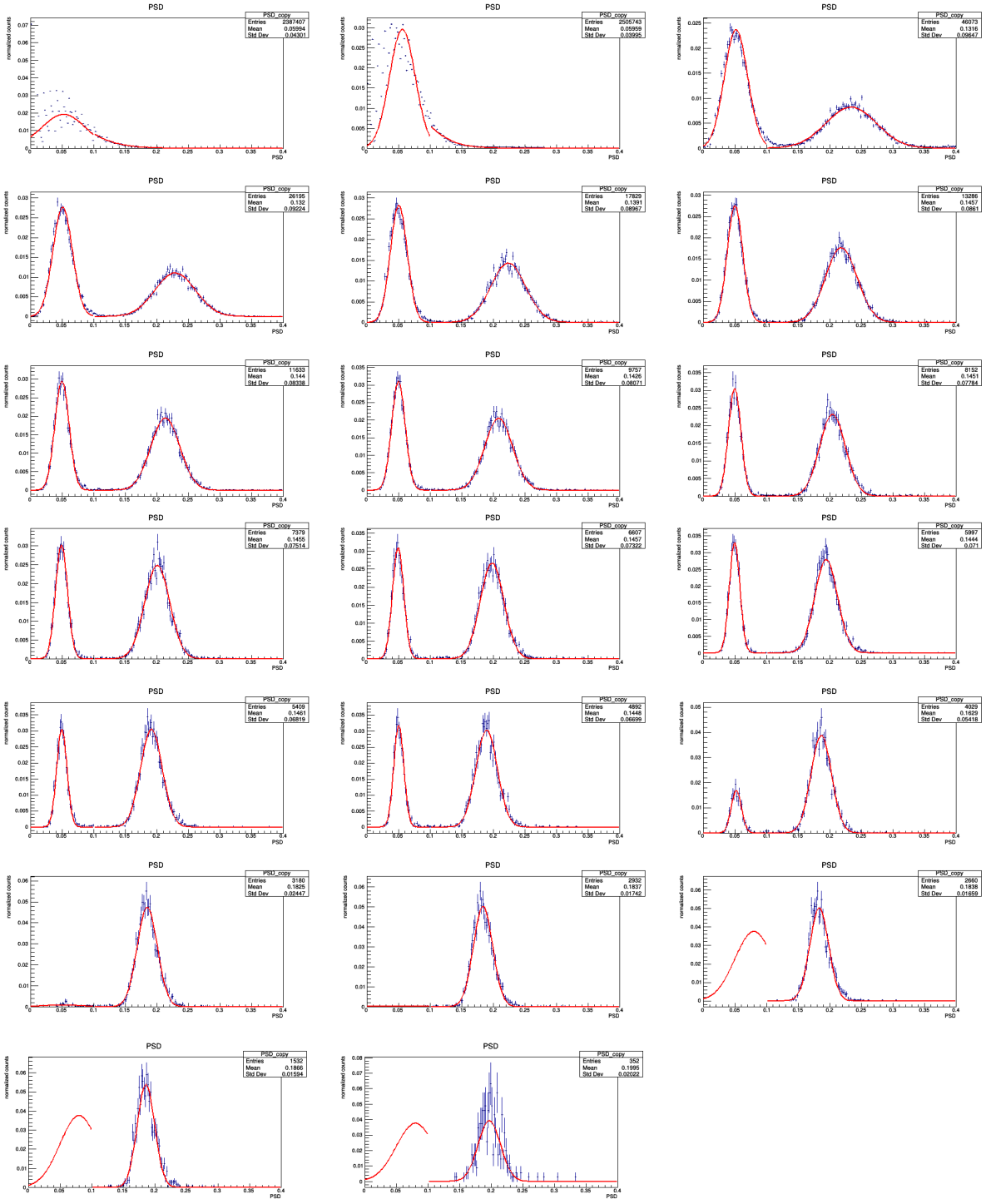

Figure 10.3: Nuclear and electronic recoil peak for each energy interval. The x-axis shows the PSD value and the y-axis the normalized count. The plot at the top left corresponds to the energy interval of 0-100 ADC. It then goes on in 100 ADC steps from the top left to bottom right with the last energy interval at 1900-2000 ADC. With this overview one can estimate the fit ranges and fit parameters as well as which energy intervals have to be excluded.

Part IV

Safe solvents

11 Definition and state-of-the-art

Today, liquid scintillators are widely used in large scale facilities like Borexino [33] and KamLAND [34]. They also find application in e.g. homeland security, medicine and material characterization. Traditionally, liquid scintillators were based on benzene, toluene, xylene, or pseudocumol due to their high performence but with the drawback of safety issues. For large scale facilities of the new generation new aromatic solvent candidates like LAB, DIN and PXE, which are classified as safer solvents, have been investigated.

11.1 Scintillator standards

Aromatic organic solvents have proven to be the best solvents for liquid scintillation counting due to their high light yield. Traditional solvents are p-Xylol, Pseudocumol and similar variants.

Mixture	**LY**	**rel. LY**	**FoM$_{max}$**	**rel. FoM$_{max}$**
EJ301	1133	1.296	2.357	1.997
p-Xylol(4g/l PPO, 10mg/l POPOP)	1121	1.283	1.710	1.449
MP363(8% Naphthalene)	1112	1.272	2.201	1.865
MP363	997	1.141	2.123	1.799
MP363(4% Naphthalene)	992	1.135	2.001	1.696
MP363(16% Naphthalene)	969	1.109	2.079	1.762
MP363(6% Naphthalene)	954	1.092	1.955	1.657
MP363(10% Naphthalene)	930	1.064	2.034	1.724
BC501A	918	1.050	2.339	1.982
LAB(4g/l PPO, 20mg/l POPOP)	874	1.000	1.180	1.000
MP363(12% Naphthalene)	874	1.000	1.848	1.566

Table 11.1: Measurements of the light yield and PSD of classical liquid scintillators compared to the common safe scintillator LAB. MP363 is a xylol based scintillator with 0.4% PPO and 0.001% POPOP.

In Table 11.1 light yield and PSD capability are shown for different liquid scintillators. The scintillator EJ301 [C9] is a scintillator from Eljen Technology, BC501A [C10] is from Saint-Gobain, which was stored in the laboratory for several years. EJ301 and BC501A are chemically similar xylol based scintillators with admixtures of naphthalene. MP363 is a scintillator mixed at the MPIK. The interpretation of results on the MP363 samples with different naphthalene concentration is difficult

since no trend could be observed and the values, in particular the light yield, were fluctuating and hard to reproduce. Our hypothesis is that the different samples did not have the expected concentrations due to incomplete dissolution not visible by eye. The naphthalene concentration of 8% with 0.4% PPO and 0.001% POPOP corresponds to EJ301 and BC501A. At this concentration slightly lower, but similar values were obtained for MP363 and EJ301. BC501A showed a significant lower light yield, probably due to aging effects.

Even though the light yield and PSD of classical solvents is high, there is a drawback, mainly the low flash point[1] [36]. p-Xylol has its flash point at 24°C and Pseudocumol at 48°C and these solvents are therefore classified flammable [C2] [C3]. Other problems are the high vapour pressure (p-Xylol: 8.7 hPa at 20°C, Pseudocumol: 2.8 hPa at 25°C), toxicity, hazardous for human health and harmfulness for the environment. These are the reasons why the demand for safer solvents increased in the last years.

11.2 Safe solvents

Safe solvents have a high flash point of about 100°C or above, low vapour pressure and low toxicity. The most common safe solvents are LAB, DIN and PXE. Some of their main properties are listed in Table 11.2.

Solvent	ρ [g/cm^3]	Flash point [°C]	Vapour pressure [Pa]	Refractive index[2]
LAB	0.86	140-145.5	1.3 (20°C)	1.4828 (20°C)
DIN	0.958	> 140	0.5 (20°C)	1.565
PXE	0.98	167.1	0.133 (25°C)	1.56-1.57 (25°C)

Table 11.2: Physical and chemical properties of selected safe solvents [C11] [C12] [C13].

The DIN in Table 11.2 is a mixture of isomers, which means a mixture of compounds with the same chemical formula but different structural arrangements [41]. We defined LAB with 4g/l PPO as primary fluor and 20mg/l POPOP as secondary fluor as our standard scintillator. All measurements of light yield and PSD of other scintillator samples are given relative to the standard scintillator. Also, all measurements of light yield and PSD are assumed to have the same relative error of $\frac{\Delta \mathrm{LY}}{\mathrm{LY}} = 0.024$ and $\frac{\Delta \mathrm{FoM_{max}}}{\mathrm{FoM_{max}}} = 0.01$. The LY and PSD of LAB as a reference value is assumed to be fixed due to the fact that it is the average of multiple measurements and therefore has a much lower error than the other samples.

[1] the lowest temperature at which vapours above a volatile combustible substance ignite in air when exposed to flame [35]

[2] Refractive indices: [C14] [C15] [C16]

11.2.1 LAB

LAB is classified as hazardous for human health, but has an attenuation length at 430 nm of more than 10 meters, which is important in large detectors because the scintillator has to be transparent to light around that wavelength, such that it can reach the PMT at its maximum efficiency region. LAB was first proposed in the context of the SNO+ (Sudbury Neutrino Observatory plus) experiment [37] and is the scintillator basis of many recently running or upcoming neutrino experiments as Daya Bay [38], RENO [39] and JUNO [40].

I tried to find a mixture of LAB with a higher light yield and PSD than our standard scintillator by fluor variation and admixtures of other solvents (Table 11.3).

Mixture	**LY**	**rel. LY**	**FoM$_{max}$**	**rel. FoM$_{max}$**
LAB(4g/l PPO, 20mg/l POPOP)	874	1.000	1.180	1.000
LAB(PPO, Bis-MSB)	853	0.976	1.222	1.036
LAB(3g/l PMP)	812	0.929	1.007	0.853
LAB+2,6DIN(90:10, PPO, POPOP)	580	0.664	1.391	1.179
LAB+oil(20:80, PPO, POPOP)	471	0.539	-	-

Table 11.3: Different mixtures of LAB (the oil is paraffin oil). All samples including PPO have fluor concentrations of 4 g/l and all samples with secondary wavelength shifter (POPOP or Bis-MSB) 20 mg/l.

The scintillator of LAB with the fluor PMP[3] does not need a secondary fluor due to the large stokes shift with an absorption maximum at 295 nm and an emission maximum at 425 nm [42], which has a large overlap with the emission spectrum of LAB (Table 11.6). The mixture with 2,6DIN, which is a specific solid DIN isomer [C17], has a higher PSD but a much lower light yield. The notation x:y e.g. 90:10 means 90% of the first named solvent and 10% of the second named solvent (all percentages are given in % weight). The mixture of LAB and paraffin oil was measured to get an estimation of the light yield of the NoWaSH (New opaque Wax Scintillator, Heidelberg) scintillator. NoWaSH is an opaque scintillator with a mixture of LAB and paraffin wax, which uses optical fibers to detect the light close to the interaction point [43]. Due to transparency, we used paraffin oil instead of wax. POPOP has its absorption maximum at 360 nm and Bis-MSB at 345 nm, while PPO has its emission maximum at 358 nm [44]. This might be the the reason for the slightly better LY and PSD with POPOP, although the difference is not very significant. Moreover, I tried a mixture of LAB and DIN with 4g/l PPO and 10 mg/l POPOP (Table 11.4).

[3] 1-Phenyl-3-mesityl-2-pyrazolin

Mixture	LY	rel. LY	$\mathbf{FoM_{max}}$	rel. $\mathbf{FoM_{max}}$
LAB(4g/l PPO, 20mg/l POPOP)	874	1.000	1.180	1.000
DIN(4g/l PPO, 10mg/l POPOP)	1018	1.165	2.010	1.703
LAB(4g/l PPO, 10mg/l POPOP)	798	0.913	1.089	0.923
LABDIN(98:2)	759	0.868	1.186	1.005
LABDIN(95:5)	774	0.886	1.331	1.128
LABDIN(90:10)	822	0.941	1.452	1.231
LABDIN(85:15)	794	0.908	1.515	1.284
LABDIN(80:20)	814	0.931	1.504	1.275
LABDIN(50:50)	949	1.086	1.604	1.359
PXE(4g/l PPO, 10mg/l POPOP)	941	1.077	1.224	1.037

Table 11.4: Mixture of DIN and LAB

The scintillator with the solvent DIN has a higher light yield and PSD than pure LAB. It is also higher than PXE especially in the PSD. The light yield of the mixtures increases linearly with the DIN concentration as shown in Figure 11.1.

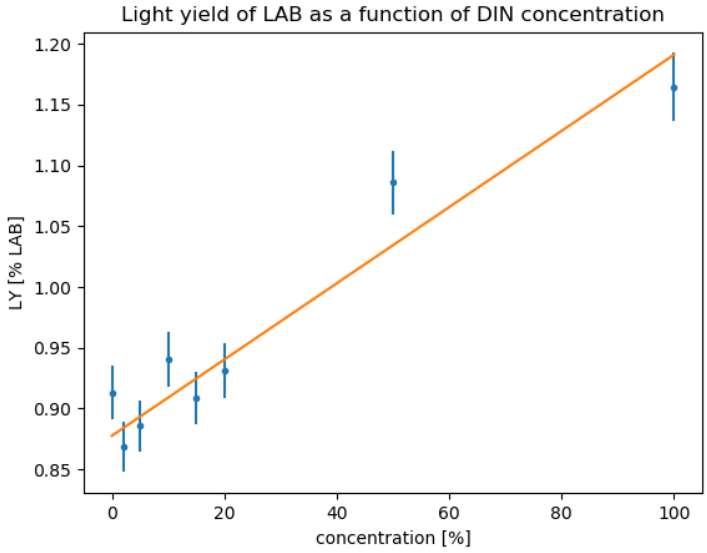

Figure 11.1: Linear fit of the LAB+DIN mixtures (light yield is given in % of the standard scintillator). The point at zero percent concentration was excluded from the fit due to the fact that the the light yield at low concentrations decreases compared to pure LAB. A possible reason for the decrease in light yield at low DIN concentrations might be losses due to the opening of new energy transfer paths. The linear fit gives the slope $a = 0.030 \pm 0.004$, the vertical intercept at $b = 0.888 \pm 0.014$ and $\chi^2_{red} = 1.63$.

11.2.2 DIN

DIN is classified as hazardous for human health and harmful for the environment. The attenuation length of the MPIK sample (Rütgers) at 430 nm was measured to be 1.2 m as received and 1.7 m after Al_2O_3 column purification [67]. To optimize the light yield and PSD, I measured scintillator samples with different primary fluors (PPO, BPO, PBD, butyl PBD and DPA)[4] to find the best overlap with the secondary fluor POPOP. The results of these studies are summarized in Table 11.5.

Mixture	**LY**	**rel. LY**	**FoM$_{max}$**	**rel. FoM$_{max}$**
LAB(4g/l PPO, 20mg/l POPOP)	874	1.000	1.180	1.000
DIN(POPOP)	400	0.458	-	-
DIN(4g/l PPO, POPOP)	1018	1.165	2.009	1.703
DIN(4g/l BPO, POPOP)	1052	1.204	1.837	1.557
DIN(4g/l PBD, POPOP)	651	0.745	1.601	1.357
DIN(4g/l butyl PBD, POPOP)	824	0.943	1.744	1.478
DIN(4g/l DPA)	543	0.621	-	-
Ultima Gold F	956	1.094	1.775	1.504

Table 11.5: DIN with different primary fluors. All samples of DIN including POPOP have fluor concentrations of 10 mg/l.

Ultima Gold F is a DIN based commercially scintillator (Perkin Elmer [C18]). The attenuation length of the Ultima Gold F sample is about 0.7 m, which is low compared to the attenuation length our DIN sample. This could explain the relative low light yield and PSD of Ultima Gold F. DIN with the primary fluor DPA does not need a secondary fluor just like PMP, but it has a low light yield and due to the bad pulse shape discrimination no measurable PSD value.

Molecule	**abs. max.**	**em. max.**	**Quantum yield**
POPOP	360 nm	411 nm	0.90 ± 0.05
PPO	303 nm	358 nm	0.836 ± 0.043
BPO	320 nm	384 nm	0.91 ± 0.05
PBD	302 nm	358 nm	0.84 ± 0.05
butyl PBD	302 nm	361 nm	0.89 ± 0.05
DPA	373 nm	407 nm	0.91 ± 0.05
LAB	260 nm	284 nm	0.20 ± 0.02
DIN	279 nm	338 nm	0.32 ± 0.03

Table 11.6: Quantum yield, absorption and emission maxima of the different molecules [44].

Table 11.6 explains why DPA has the lowest light yield of all measured fluors despite

[4] [C4], [C19] - [C22]

the highest quantum yield due to the fact that the absorption spectrum of DPA has a smaller overlap with the emission spectrum of DIN than the other fluors. Even though the other four fluors have similar absorption and emission maxima, they differ in light yield and PSD. The reason for that is that not just the position of the maxima is important, but the overlap of the whole absorption and emission spectra. Therefore, PPO and BPO have the highest light yield and PSD capability. From an energy transfer point of view not the mass concentration but the molar concentration should be compared. The different fluor masses differ up to a factor of 1.6. Still we do not expect PBD and butyl PBD to catch up that much after a correction of the concentration. Also important is the quantum yield of the different fluors. BPO and DPA have an especially high quantum yield. PPO has the lowest quantum yield of all measured fluors, but still gives a good result due to previously mentioned criteria.

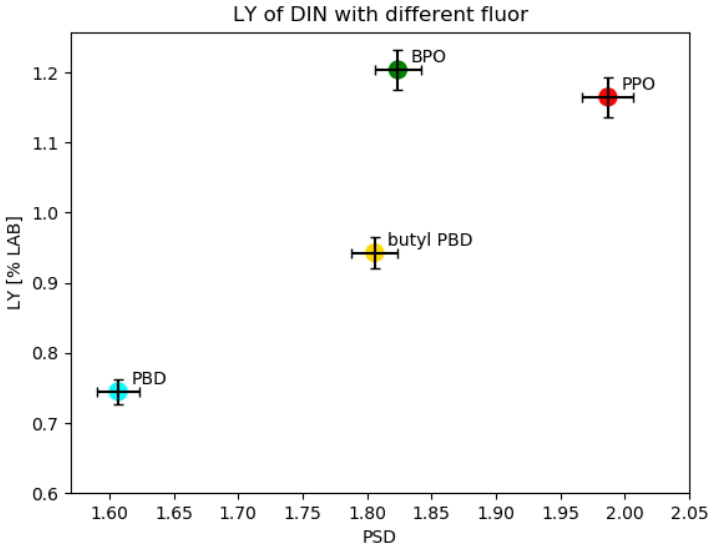

Figure 11.2: Light yield and PSD of the samples with different primary fluor. The PSD value is the asymptotic maximum of the FoM.

BPO and PPO have a similar light yield (within the error) but PPO has a higher PSD, which makes it overall the best primary fluor for DIN. To find out if we can increase the PSD with a different concentration of PPO I measured a few samples of different PPO concentration.

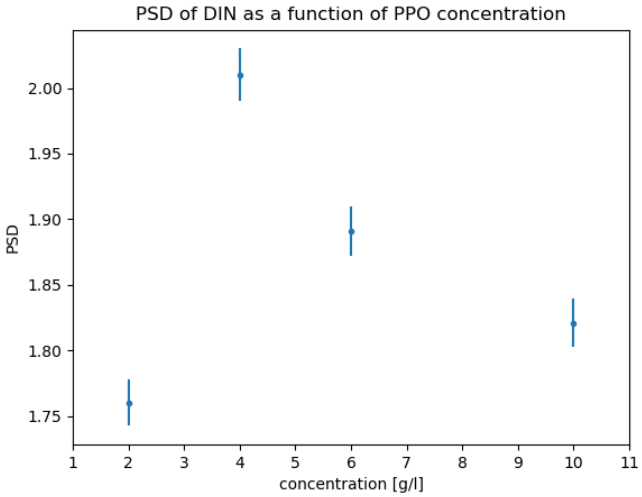

Figure 11.3: Samples of DIN with different PPO concentration

Figure 11.3 shows that 4g/l PPO has the highest PSD value of all measured samples. So it seems like we already had the concentration with the best PSD capability. To get a more accurate result we could have done a scan with a lower concentration step size, but given the rather weak concentration dependence it was accurate enough to know the maximum is around 4g/l. This concentration is also optimal for light yield (Figure 11.4).

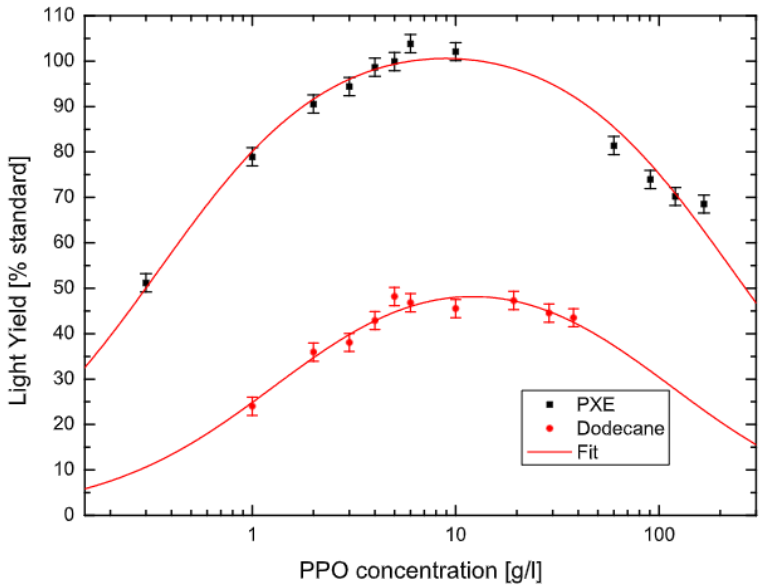

Figure 11.4: Variation of PPO concentration in PXE and dodecan. The light yield is given relative to the standard: PXE plus 6 g/l PPO. The function A.16 is fitted. [45]

DIN and PXE should have a similar response to variation of PPO concentration. PXE as shown in Figure 11.4 has its maximum around 4 g/l to 10 g/l, which is the reason why we did not study PPO concentrations outside the 2 g/l to 10 g/l region. If the PPO concentration is too low or too high the light yield decreases due to too low molar concentration and self-quenching of PPO respectively, where an unexcited and an excited PPO molecule interact and the excitation energy is lost by collision.

11.2.3 1-Methylnaphthalene

1-Methylnaphthalene (MN) is hazardous for human health and harmful for the environment. It has an attenuation length of 0.19 m to 1.11 m at 430 nm before and after Al_2O_3 column purification, a flash point of 82°C, a density of 1.024 g/cm^3 [C23] (no data available for the vapour pressure) and a refractive index of 1.6120-1.6180 (20°C) [C24]. It has its absorption maximum at $\sim$ 282 nm and its emission maximum at $\sim$ 345 nm and [46], which is the reason why we chose a single fluor mixture with POPOP as the fluor (Table 11.7).

Mixture	**LY**	**rel. LY**	**FoM$_{max}$**	**rel. FoM$_{max}$**
LAB(4g/l PPO, 20mg/l POPOP)	874	1.000	1.180	1.000
MN(0.005g/l POPOP)	481	0.550	-	-
MN(0.01g/l POPOP)	494	0.565	-	-
MN(0.1g/l POPOP)	860	0.984	-	-
MN(0.2g/l POPOP)	988	1.130	-	-
MN(0.5g/l POPOP)	1066	1.220	1.540	1.305
MN(0.1g/l POPOP, 3g/l PPO)	983	1.125	-	-
MN(0.5g/l POPOP, 3g/l PPO)	1017	1.164	-	-

Table 11.7: Different samples of MN

I only measured the PSD for the sample with the highest light yield. Table 11.7 also shows that our expectation was correct that we only need POPOP and no additional primary fluor. The reason why the sample with 0.1 g/l POPOP increases in light yield if we add 3g/l PPO is probably because the fluor concentration of POPOP alone is too low for an optimal energy transfer. Which would fit to the result of the sample with 0.5 g/l POPOP, which has the optimal concentration and therefore decreases if we add PPO. The light yield of MN depending on the concentration of POPOP can be described with Equation 2.1:

$$\mathrm{LY}_{rel} = \frac{A}{1 + c_0/c} + B \tag{11.1}$$

where c_0 is the critical concentration and A and B are free parameter. Figure 11.5 shows the fit of the light yield depending on the POPOP concentration.

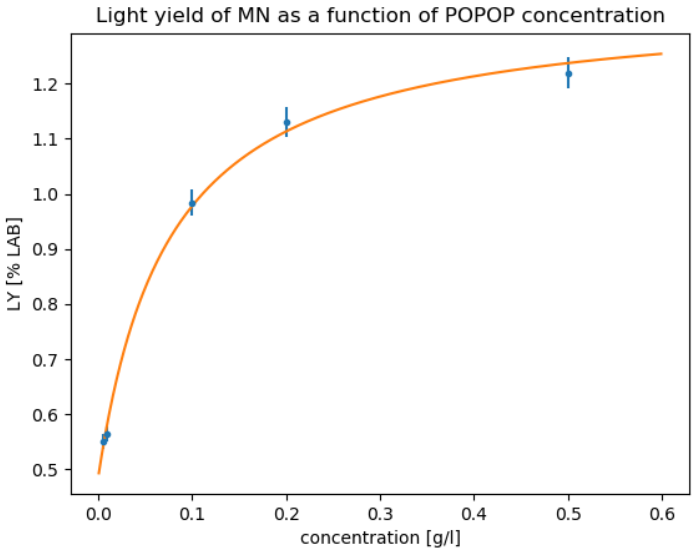

Figure 11.5: Light yield function of MN. The critical concentration is $c_0 = 0.08 \pm 0.02$ g/l and $A = 0.87 \pm 0.06$, $B = 0.48 \pm 0.02$. The reduced chi-squared is $\chi^2_{red} = 1.29$.

The highest light yield of the MN samples has a slightly higher light yield than the DIN sample with 4 g/l PPO but a much lower PSD. This and the fact that MN has a relative low flash point compared to DIN makes DIN the better option. Moreover, MN was reported to be rather sensitive to optical degradation as compared to other solvents [47]. Nevertheless, the option of having a high light yield scintillator, with a simple two component system at low fluor concentration is appealing.

11.2.4 Phenylsiloxane

To increase the detection efficiency in many cases large size detectors are needed with the extreme example of tens of thousands of cubic meters of liquid scintillator. In this framework, the issues connected with liquid toxicity, volatility and flammability of solvents can not be ignored. Moreover, these detectors might be placed at sites with strict safety constraints as underground laboratories. Therefore, traditional safe solvents could not be safe enough. Siloxane based liquid scintillators should be even safer due to their very high flash point, very low volatility, inertness, stability at room temperature and simple disposal. Siloxane compounds can be produced in a wide range of structures, thus allowing to fulfill the requirements regarding optical and chemical properties [48] [49]. After interesting results achieved with polysiloxane based plastic scintillators, also polysiloxane based liquid scintillators have been tested [50]. Therefore in this framework, we studied three different phenylsiloxanes: Polymethylphenylsiloxane (PMPS) [C25], 1,1,5,5-Tetraphenyl–1,3,3,5- tetramethyl trisiloxane (TPTMTS) and 1,1,3,5,5-pentaphenyl1,3,5-trimethyltrisiloxane (PPTMTS). TPTMTS and PPTMTS were produced via the company Sindlhauser Materials

GmbH, which sells them under the tradename S-04V and S-05V as oil for diffusion pumps [C26]. Some of the main properties are listed in Table 11.8.

Solvent	ρ [g/cm^3]	Flash point [°C]	Vapour pressure [Pa]	n	η [mm^2/s]
PMPS	1.11	300	NA	1.53	500
S-04V	1.07	> 230	$5 \cdot 10^{-5}$ (20°C)	1.55	33
S-05V	1.09	243	$3 \cdot 10^{-8}$ (20°C)	1.58	175

Table 11.8: Physical and chemical properties of polysiloxane samples [C25] [C26] [48] [49]. ρ is the density, n the refractive index and η the viscosity. None of them has a GHS[5] pictogram, which are hazard symbols.

Even compared to other safe solvents the flash point of the phenylsiloxanes is very high and the vapour pressure extremely low. Moreover, they have a high density compared to the previously mentioned safe solvents and no GHS hazard symbols. The viscosity of the phenylsiloxanes are rather high compared to e.g. DIN with $\eta = 6.25$ mm^2/s [C17]. S-04V has the lowest viscosity of the three phenylsiloxanes.

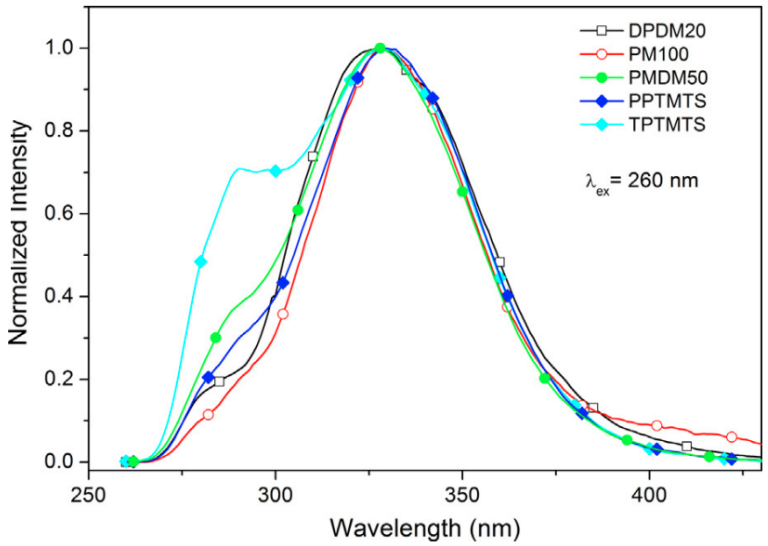

Figure 11.6: Emission spectra of the different phenylsiloxanes: PMPS is PM100, S-04V is TPTMTS and S-05V is PPTMTS [48].

Figure 11.6 shows that the emission maxima is for all three phenylsiloxanes at ~ 333 nm, but S-04V has a second smaller peak at ~ 287 nm. First, I measured different samples with PPO and POPOP (Table 11.9).

[5]Globally Harmonized System of Classification and Labelling of Chemicals

Mixture	LY	rel. LY	$\mathbf{FoM_{max}}$	rel. $\mathbf{FoM_{max}}$
LAB(4g/l PPO, 20mg/l POPOP)	874	1.000	1.180	1.000
S-04V(1%PPO, 20mg/l POPOP)	736	0.842	1.019	0.864
S-05V(1% PPO, 20 mg/l POPOP)	671	0.768	0.920	0.780
S-04V(0,5%PPO, 20mg/l POPOP)	670	0.767	0.879	0.745
S-05V(0,5% PPO, 20 mg/l POPOP)	581	0.665	0.637	0.540
PMPS(1% PPO, 20mg/l POPOP)	539	0.617	0.662	0.561
PMPS(3g/l PPO, 20mg/l POPOP)	384	0.439	-	-

Table 11.9: Different samples of PMPS, S-04V and S-05V with PPO and POPOP.

The measurements show that S-04V has the highest light yield and PSD of all measured samples. One reason for that is the high viscosity of PMPS and S-05V. PMPS has a higher viscosity than S-05V and also a lower light yield. Diffusion processes are important for the energy transfer and therefore for the light yield (chapter 2), which get limited by the high viscosity of the solvents. Also, the broad emission spectrum of S-04V compared to the other phenylsiloxanes increases the light yield of the S-04V based scintillator.

Therefore, we focused on S-04V in the further studies and measured samples with different primary fluors (Table 11.10). The attenuation length of the unfiltered and unpurified S-04V was determined to be 5.7 m at 430 nm.

Mixture	LY	rel. LY	$\mathbf{FoM_{max}}$	rel. $\mathbf{FoM_{max}}$
LAB(4g/l PPO, 20mg/l POPOP)	874	1.000	1.180	1.000
S-04V(1,2% butyl PBD, POPOP)	849	0.971	1.075	0.911
S-04V(0,8% PMP)	833	0.953	1.009	0.855
S-04V(0,8% butyl PBD, POPOP)	828	0.947	0.939	0.796
S-04V(0,61% NPO, POPOP)	817	0.935	1.018	0.863
S-04V(0,67% BPO, POPOP)	806	0.922	1.029	0.872
S-04V(0,4% PMP)	738	0.844	0.685	0.581
S-04V(1%PPO, POPOP)	736	0.842	1.019	0.864
S-04V(0,4% butyl PBD, POPOP)	735	0.841	0.690	0.585
S-04V(0,5%PPO, POPOP)	670	0.767	0.879	0.745
S-04V(0,2% PMP)	594	0.680	-	-
S-04V(0,3% NPO, POPOP)	549	0.628	0.858	0.727

Table 11.10: Samples of S-04V with different primary fluors and concentration. All samples of S-04V with POPOP have a fluor concentration of 20 mg/l.

The best options seem to be butyl PBD and PMP with identical light yield within error and slightly different PSD. PMP has an about $(6.5 \pm 1.5)\%$ worse PSD than the best butyl PBD but has the advantage of not needing a secondary fluor. Moreover, at the identical fluor concentration by weight of 0.8% the scintillator with PMP

performs even better. However, higher PMP concentration do not improve the situation. The sample with butyl PBD and the standard scintillator LAB have a similar light yield, but LAB has an about $(9.8 \pm 1.0)\%$ higher PSD than butyl PBD. The fluor NPO has its absorption maximum at about 334 nm and the emission maximum at about 398 nm [51]. Even though the absorption has a good overlap with the emission of S-04V it does not have an outstanding light yield. This is caused by the rather small overlap with POPOP, but without a secondary fluor the emission wavelength is a little bit too low causing self-absorption in the liquid scintillator.

11.3 Discussion

A summary of the results is shown in Figure 11.7 and Table 11.11.

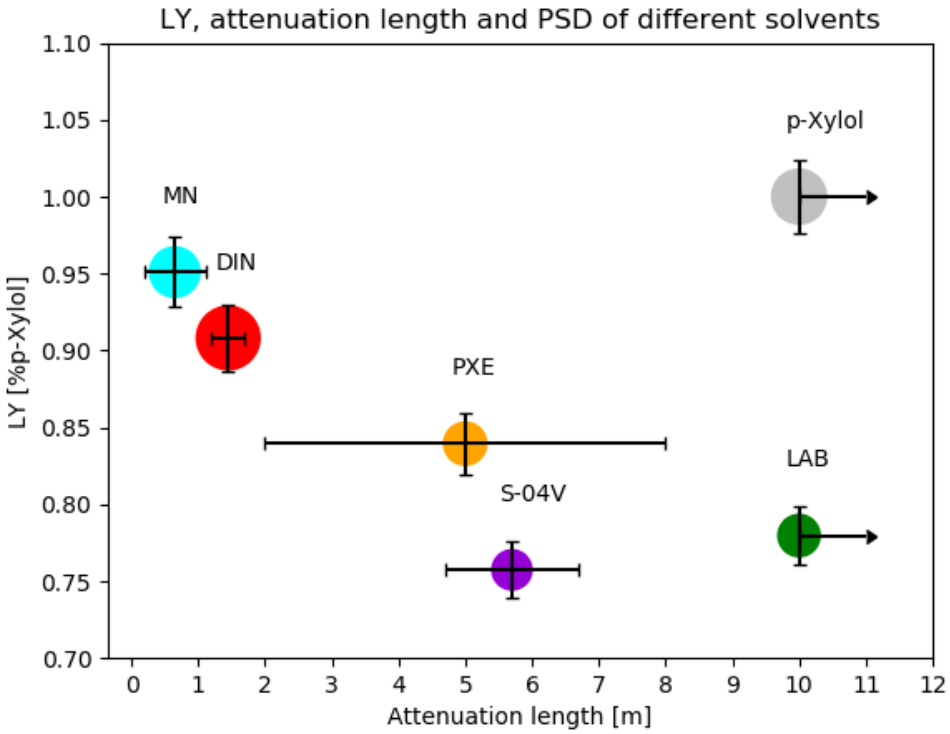

Figure 11.7: Best sample of each safe solvent compared to the classical solvent p-Xylol. The errorbars of the attenuation length show the variation range before and after Al_2O_3 column purification. For S-04V the attenuation length is the measured value before column purification. The arrows of LAB and p-Xylol show that the attenuation length is greater than the given value, since above 10 m the UV/Vis spectrometer starts to loose its sensitivity. The point size scales with PSD capability.

Mixture	**rel. LY**	**rel. FoM$_{max}$**	**Λ[m]**
p-Xylol(4 g/l PPO, 10 mg/l POPOP)	1	1	>10
MN(0.5g/l POPOP)	0.951	0.901	0.19-1.11
DIN(4g/l PPO, 10mg/l POPOP)	0.908	1.175	1.2-1.7
PXE(4g/l PPO, 10mg/l POPOP)	0.839	0.716	2-8
LAB(4g/l PPO, 20mg/l POPOP)	0.780	0.690	>10
S-04V(1,2% butyl PBD, 20mg/l POPOP)	0.757	0.629	5.7 ± 1.0

Table 11.11: List of the best sample of each safe solvent compared to p-Xylol. Λ is the attenuation length in metre.

It turned out that three of the safe solvent have to be highlighted: DIN, LAB and the polysiloxane based S-04V. Each of them has its strength in a different application. DIN has a high light yield comparable to MN but distinguishes itself with a very good PSD from the others. But it also has disadvantages, especially the rather small attenuation length. Moreover, it is classified as hazardous for human health and harmful for the environment. A rather small detector, where the attenuation length and the hazards are no problem and which needs a good energy resolution and pulse shape discrimination to differentiate between different ionizing particles would perfectly fit for a DIN based scintillator.

LAB on the other hand has a worse light yield and PSD than DIN but has a more than five times larger attenuation length. It is similar to PXE in light yield and PSD but does not have the downside of being harmful for the environment like PXE, MN and DIN. It is suitable for large detectors, which do not need such a high light yield and PSD like a DIN based scintillator.

S-04V has a similar light yield and PSD as LAB, but about half of the attenuation length. But S-04V was not purified and the chemical purity is not specified by Sindlhauser Materials GmbH. Therefore, S-04V has a high potential for larger attenuation lengths after purification. Its major advantages are that it has not a single GHS pictogram and its high flash point and very low vapour pressure even compared to other safe solvents. An S-04V based scintillator would fit a detector, where safety is the most important criterium and energy resolution and pulse shape discrimination are rather of secondary importance.

12 Muon-flux measurements with new polysiloxane based scintillator

As an application for the polysiloxane (S-04V) based scintillator, I performed a muon-flux measurement in different rooms at the Max-Planck-Institut für Kernphysik (MPIK). Due to the fact that cosmic muons are high-energy particles, we can assume that they roughly lose about 2MeV/cm [2], which means they can lose up to 12 MeV in our scintillator cell. For this reason we have to reduce the power of the signal with two attenuators, which are simple voltage dividers, to avoid saturated events. The attenuators have 10db and 6db, which reduces the power of the signal to about 1/6 of its value. A simple way to estimate the muon-flux is to measure the background radiation and define a cut value to filter out natural radiation like potassium-40 (^{40}K). Therefore, I had to perform a calibration measurement with ^{137}Cs and identify the background. In Figure 12.1 one can see the identified background events. The first compton-edge is from potassium-40 (^{40}K) with $E\gamma = 1460.8$ keV [52], which corresponds to a compton-edge at $E_c = 1243.3$ keV. The second compton-edge is from thallium-208 (^{208}Tl) with $E\gamma = 2614.5$ keV [53], which corresponds to a compton-edge at $E_c = 2381.8$ keV. The cut value was placed at 500 ADC, which corresponds to about 2.5 MeV. To estimate the muon-flux, I integrated all events greater than 2.5 MeV and divided by the measuring time. To have a sufficient statistic we performed each muon-flux measurement for multiple hours.

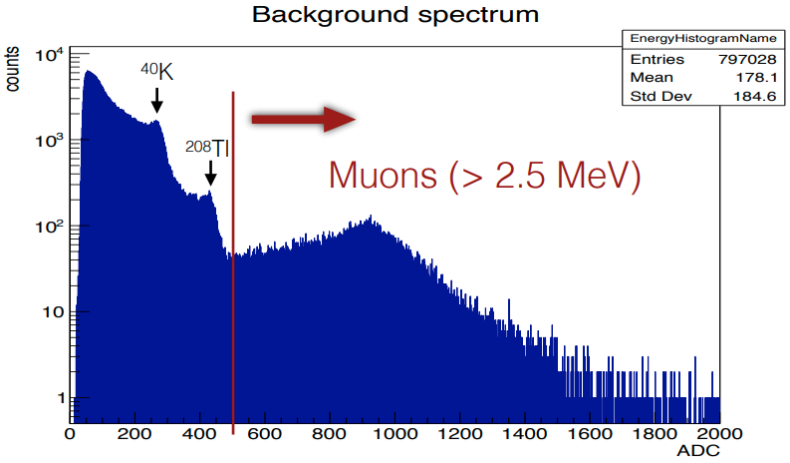

Figure 12.1: Background measurement with identified background sources and the determined cut for cosmic muons.

The first location Ge370 for the muon-flux measurement was the spectrometry lab, and the liquid container of the scintillator module was placed next to the window. In this configuration the muon-flux is effectively measured without any shielding. The next location was the Low-Level lab (LLL), which should have the highest reduction factor of all measurements. The last location was the room Ge166 with three different positions at different heights (Figure 12.2).

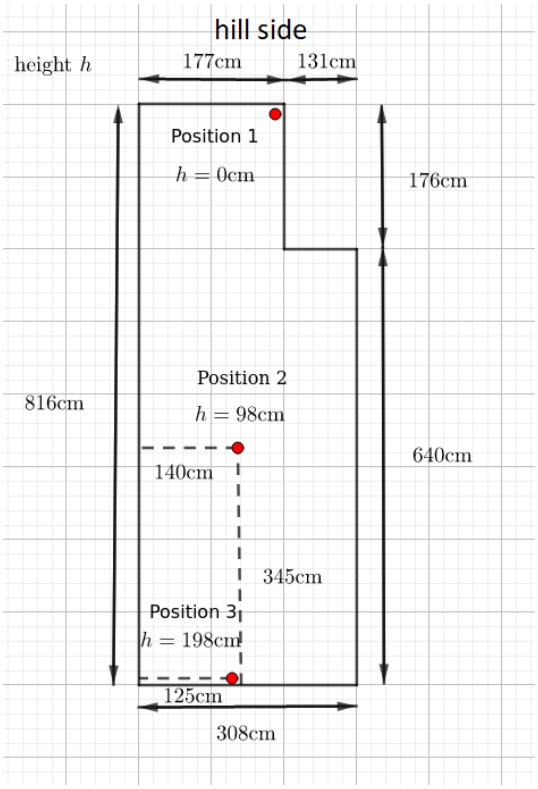

Figure 12.2: Layout of room Ge166 with the different positions.

Location	**Muon rate (Hz)**	**Reduction factor**
Ge370 (spectrometry)	0.65	1
LLL	0.25	2.6
Ge166 (position 1)	0.38	1.71
Ge166 (position 2)	0.47	1.38
Ge166 (position 3)	0.47	1.38

Table 12.1: Muon rate and reduction factor in different rooms compared to Ge370.

The measured muon rate and reduction factor of the different rooms are shown in Table 12.1. The muon-flux at the MPIK is about $200\frac{1}{\mathrm{m}^2 \cdot \mathrm{s}}$ (Figure 12.3), which leads to an expected muon rate per second in our scintillator of about 0.59 $1/s$. Our measured value in the spectrometry lab is slightly higher, but in reasonable

agreement given that the calculated value is just a rough approximation. Also, the reduction factor of the LLL matches the known reduction factor of 2-3. For the room Ge166, which is a new laboratory room at MPIK with some overburden coming mainly from the hill side, we do not have any information about the muon-flux. Our expectation for the reduction factor was that it will be between the spectrometry lab and the LLL, which is confirmed by the measurements.

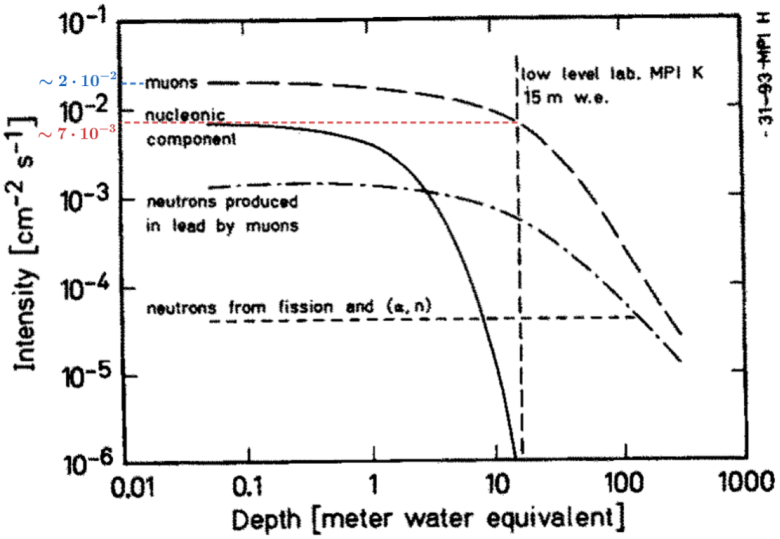

Figure 12.3: Muon-flux against depth at the MPIK (in blue muon-flux without absorption and in red muon-flux at the LLL) [54].

With a PSD cut I could also estimate the neutron rate and the corresponding reduction factor compared to the spectrometry lab (Table 12.2).

Location	**Neutron rate (Hz)**	**Reduction factor**
Ge370 (spectrometry)	0.031	1
LLL	0.010	3.1
Ge166 (average)	0.024	1.3

Table 12.2: Neutron rate and reduction factor in different rooms compared to Ge370.

The reduction factors are similar to the muon measurement, which is expected due to the fact that muon events can cause neutron events by interaction with surrounding material. Muons and neutrons are a prominent background source in neutrino experiments. Therefore, shielding and identification of them is essential to suppress the background. This is also the case for the reactor neutrino experiments of Double Chooz and STEREO, which are described in the following chapter.

Part V

Liquid scintillators for reactor neutrino experiments

13 Short introduction of experiments and techniques

Liquid scintillators are an important tool for reactor neutrino experiments. Examples are the Double Chooz and the STEREO experiments for which the MPIK Heidelberg was responsible for the scintillator production.

13.1 Double Chooz

Double Chooz is a successor of the Chooz experiment in Chooz, France. Its goal was to search for a non-vanishing value of the θ_{13} neutrino mixing angle, which is responsible for changing electron neutrinos into other neutrinos [55].

13.1.1 Neutrino oscillation

Neutrino flavour transitions have been observed in many experiments like atmospheric, solar, reactor and accelerator neutrino experiments. To explain this the simplest and most widely accepted extension to the minimal Standard Model of particle physics is to allow neutrinos to have masses and mixing. The neutrino oscillation can be described through the Pontecorvo-Maki-Nakagawa-Sakata (PMNS) unitary lepton mixing matrix. The survival probability of reactor neutrinos, which are electron antineutrinos $\bar{\nu_e}$ can be approximated for the simpler two-flavour case with the formula [56]:

$$P_{\bar{\nu_e}\to\bar{\nu_e}} \approx 1 - \sin^2(2\theta_{13}) \sin^2\left(1.267 \frac{\Delta m^2_{ee}}{4E_{\bar{\nu_e}}} L\right) \tag{13.1}$$

where L (m) is the distance, $E_{\bar{\nu_e}} = E_e^+(\text{MeV}) + 0.78\text{MeV}$ the energy of the neutrino and $\Delta m^2_{ee}(\text{eV}^2)$ is the pertinent ν_e-weighted average of Δm^2_{31} and Δm^2_{32}, which is the difference between the squared mass eigenstates 3 and 1 and 3 and 2 respectively.

13.1.2 Concept of Double Chooz

Two almost identical detectors containing about 30 cubic meters (neutrino Target and Gamma Catcher) of liquid scintillator as target were placed next to the Nuclear Power Station Chooz with a distance of 1050 m and 400 m from the two cores. The neutrino production rate of the Nuclear Power Station is about $16 \cdot 10^{20}$ per second [7]. Double Chooz is a so-called disappearance-experiment due to the fact that the neutrino oscillation leads to an disappearance of electron antineutrinos, which can

be detected by comparing the near detector flux, which measures almost the total unoscillated neutrino flux with the far detector taking into account the difference in solid angles. The electron antineutrinos are detected by inverse beta decay:

$$\bar{\nu_e} + p \rightarrow e^+ + n \tag{13.2}$$

The reaction is not sensitive to muon and tau neutrinos due to energy conservation. Therefore, the detector is blind for oscillated neutrinos of different flavours.

13.1.3 Compositions of the detectors

Both detectors (Figure 13.1) consist of the neutrino target, gamma catcher, buffer and veto system (from inside out) [55] [7].

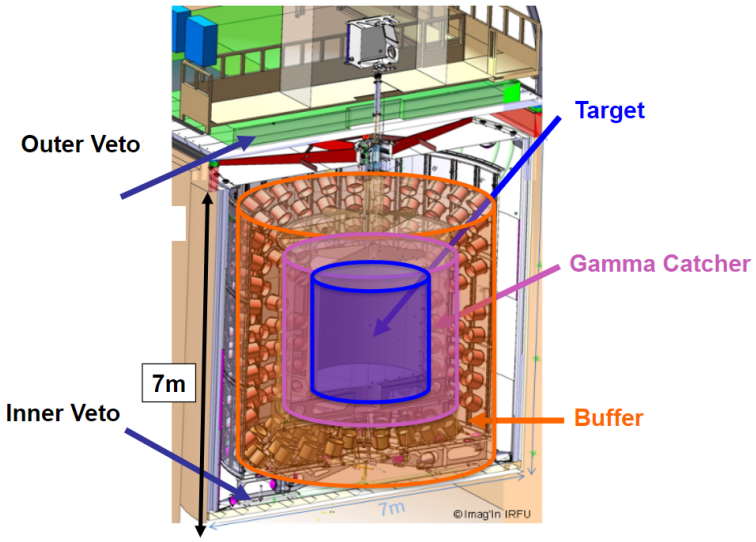

Figure 13.1: Detector design [57] (identical for near and far detector)

Neutrino target & Gamma catcher

The neutrino target (10.3 m^3) is filled with 0.1 % Gd loaded (chapter 14) liquid scintillator. The liquid scintillator is a mixture of the solvents PXE and n-Dodecan with PPO and Bis-MSB as fluors. Here the positron loses its energy by interaction with the scintillator and annihilation with an electron. The neutron thermalizes and is finally captured on gadolinium or hydrogen nuclei. This leads to two light pulses, one from the positron and a delayed pulse after neutron capture and subsequent gamma emission.

The gamma catcher (22.6 m^3) detects the photons leaving the neutrino target and therefore does not need Gd-loading. It also consists of a liquid scintillator. Although it was not planned, the GC could be finally included as neutrino target volume due to the low background achieved in the DC detectors.

Buffer

The buffer is a non-scintillating region, which aims to decrease the level of accidental backgrounds mainly from small radioactive impurities in of the 390 PMTs that are located at the buffer vessel. The PMTs convert the scintillation photons into an electrical signal.

Veto system

The inner veto is the fourth volume and consists of a LAB based liquid scintillator and 72 PMTs. It detects background events, mostly cosmic muons, and reject events in the neutrino target that are probably caused by them. On top of the detector is the outer veto (Figure 13.1) which detects muons that are closely missing the detector but can interact with materials outside the detector and produce neutrons, which can enter the neutrino target.

13.1.4 Result

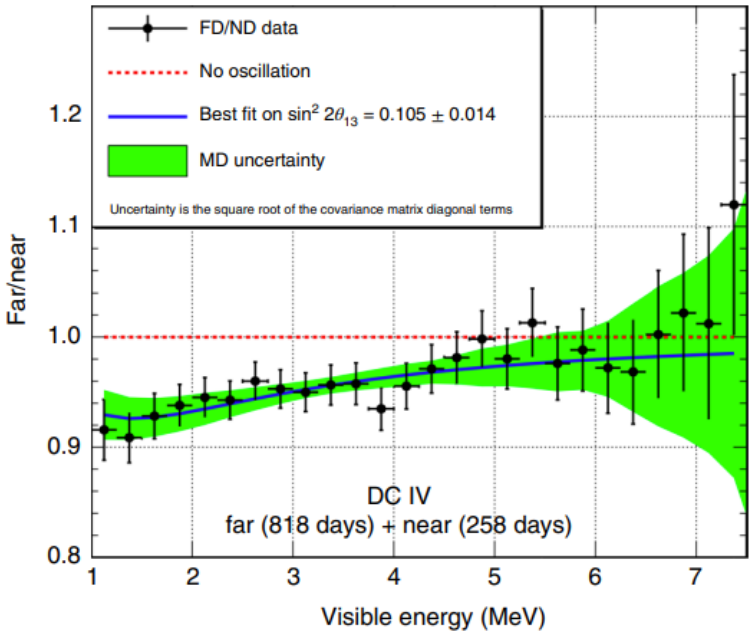

Figure 13.2: Best fit of the FD-to-ND ratio (2020) [56]

Figure 13.2 shows the ratio of the far detector (FD) to the near detector (ND) rate against the visible energy, which is $E_{vis} \approx E_{\bar{\nu}_e} - 0.78MeV$. It also shows the uncertainty of the multi-detector (MD) configuration and a red line for the no oscillation case. The mixing angle θ_{13} was determined to be [56]:

$$\sin^2(2\theta_{13}) = 0.105 \pm 0.014 \tag{13.3}$$

The result shows a clear non-vanishing mixing angle θ_{13} with a significance of 7.5σ.

13.2 STEREO

The STEREO detector was placed in Grenoble (France), at the Institut Laue-Langevin (ILL). Its goal was to reject or confirm the hypothesis of a light sterile neutrino state ($\Delta m^2 \sim 1$ eV^2) [58], which could explain the reactor antineutrino anomaly. It is a short baseline experiment with an average distance of about 10 m from the reactor core of the research reactor at ILL.

13.2.1 Reactor Antineutrino Anomaly

A deficit of about 6% of observed electron antineutrinos compared to state-of-the-art antineutrino energy spectrum calculations were found by experiments at reactors with highly and lowly enriched ^{235}U fuel. This discrepancy is known as the Reactor Antineutrino Anomaly (RAA). One explanation for this observed deficit is the existence of a fourth sterile neutrino state.

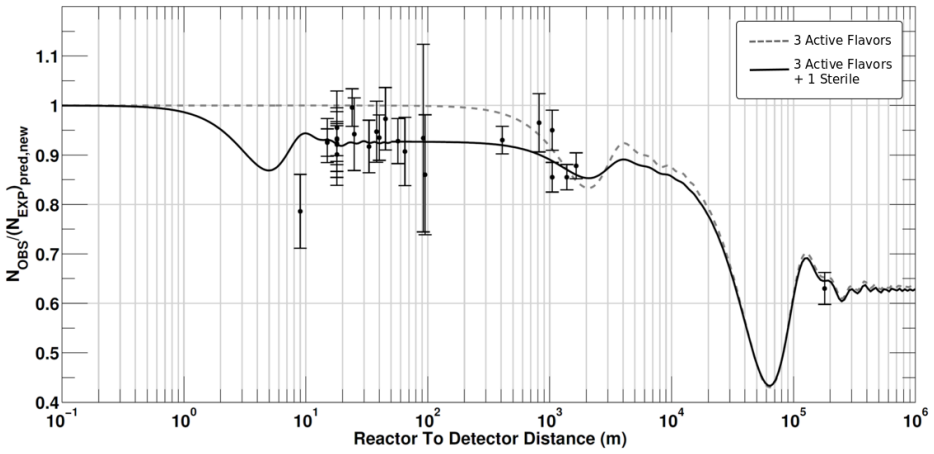

Figure 13.3: Electron antineutrino survival probability of different models and data [59].

13.2.2 Detector compositions

STEREO measured the rate as well as the relative deformation of the electron antineutrino spectrum along the detector (Figure 13.4). As in Double Chooz, the detection uses the inverse beta decay in a Gd loaded (chapter 14) liquid scintillator. The STEREO detector consists of the neutrino target, gamma catcher, buffer, water Cherenkov detector and detector shielding [60] [61].

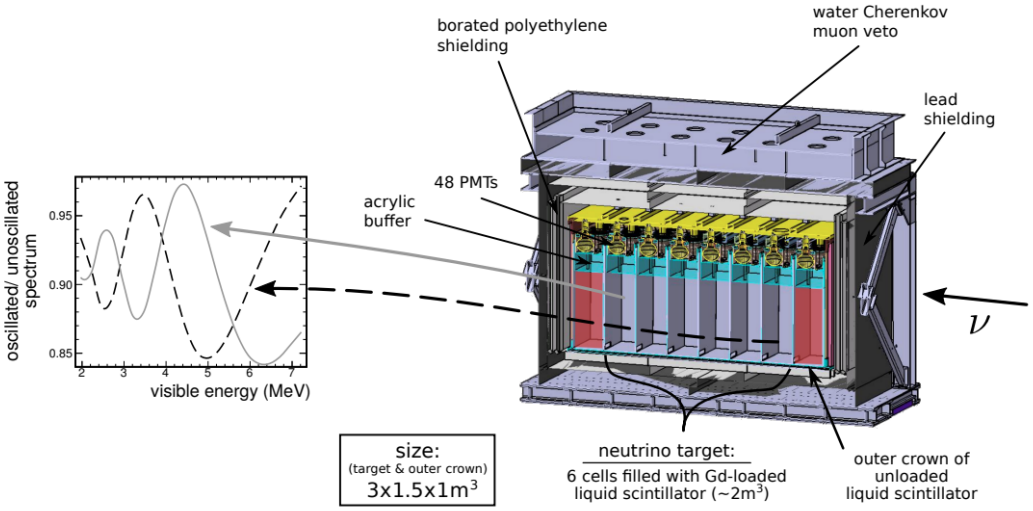

Figure 13.4: Design of the Stereodetector [60]

Neutrino target & Gamma catcher

The target is the centrepiece of the STEREO detector, consisting of six cells each with a volume of $38 \times 90 \times 90$ cm^3. It is filled with a Gd loaded liquid scintillator, which is needed to efficiently detect the neutrons produced by the inverse beta decay. Each cell is optically separated from each other, such that STEREO can measure the neutrino spectrum for each cell individually.

The gamma catcher surrounds the neutrino target and is filled with a Gd free liquid scintillator. It consists of four cells one for each side, which detect the gammas escaping the neutrino target.

Buffer

The buffers contain the 48 PMTs, which readout the light produced in the neutrino target and gamma catcher. The PMTs are separated by a layer of acrylics and buffer oil from the neutrino target and gamma catcher. The acrylic is used as a shielding and the buffer oil as an optical coupling material.

Water Cherenkov detector & shielding

Background suppression is needed due to the high background caused by cosmic muons, the research reactor and nearby experiments. Therefore, a water Cherenkov detector is located at the top of the detector to detect the cosmic muons and act as a muon veto. Also, the detector is covered by many shielding layers, accumulating to a total shielding material of 72 tons: 65 tons lead shielding, 6 tons polyethylene

shielding and 1 ton of B_4C. Additionally, the STEREO detector is surrounded by a magnetic shield, which eliminates magnetic stray fields of other nearby experimental setups.

13.2.3 Result

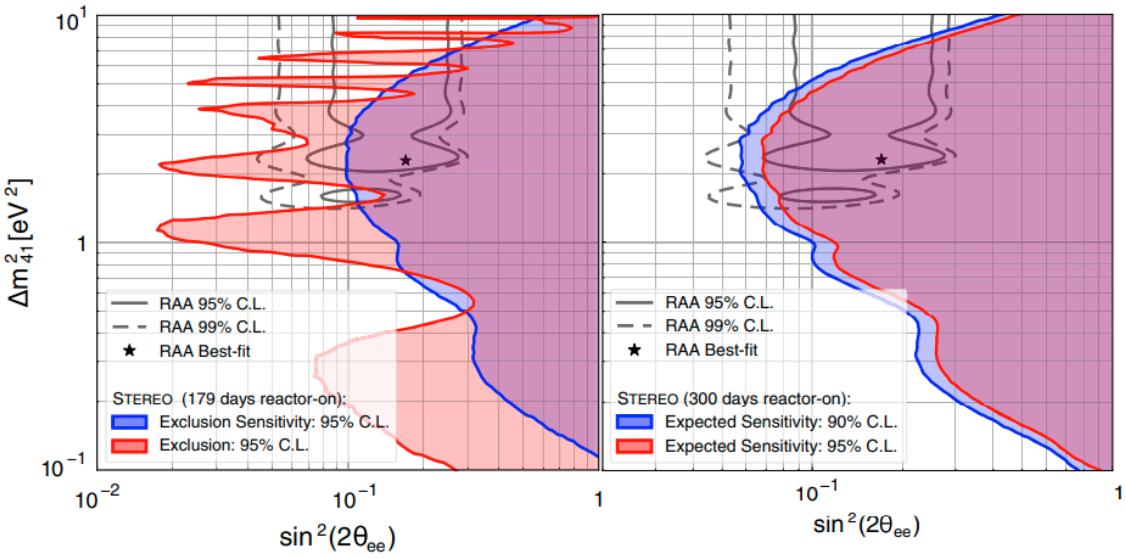

Figure 13.5: Left: Exclusion contour (red) and exclusion sensitivity contour (blue) at 95% C.L.. Overlaid are the allowed regions of the RAA (grey) and its best-fit point (star). Right: Exclusion sensitivity contour at 90% C.L. (blue) and 95% C.L. (red) expected at the full dataset of the STEREO experiment [62].

Left of Figure 13.5 shows the result of the STEREO experiment (as of 2020). The RAA region is the region of the hypothesis of a sterile, i.e., non-weakly interacting, additional neutrino. Its best fit point is at $[\sin^2(\theta_{ee}) = 0.17, \Delta m_{41} = 2.3\ \mathrm{eV}^2]$, which is excluded at more than 99.9% confidence level (C.L.) [62]. For the final dataset it is expected that the 95% C.L. exclusion sensitivity will almost fully cover the relevant Δm^2 range of the 95% allowed region of the RAA (right of Figure 13.5).

14 Gd-loaded scintillators

The liquid scintillators of Double Chooz and STEREO have to meet basic requirements: optical stability, compatibility with detector materials, transparency, high intrinsic light yield, pulse shape discrimination, safety, radiopurity and Gd solubility.

Gadolinium (Gd) has the highest cross section for thermal neutron captures of all stable isotopes, and therefore allows to lower capture time. Furthermore, the energy of the emitted gammas of the excited Gd nucleus after neutron capture increases from 2.2 MeV for hydrogen to about 8 MeV for Gd [63]. The Gd-loading therefore decreases the coincidence time between positron and neutron and increases the delayed energy of the neutron, which promotes efficient background suppression. The fact that Gd is a metal leads to the challenges connected with metal loaded liquid scintillators (LS).

The challenge is to find a chemical complex of the metal, which dissolves in the non-polar organic LS and does not deteriorate the optical property of the LS [64]. There are different approaches to dissolve the metal in the organic LS. One possibility is to use a solvent with high solubility for polar compounds like alcohols. In Chooz the $Gd(NO)_3$ was first dissolved in hexanol and then diluted in other organic solvents [65]. But the presence of nitrate ions in the solution impaired the optical properties and chemical stability of the scintillator, which lead to a limited lifetime of the detector of about 1 year [65]. Another procedure for metal loading is the preparation of a organometallic complex, which can be dissolved in the LS e.g. carboxylic acids [66]. An alternative approach is the application of beta-diketones, which are expected to be more stable than the carboxylic acid systems [64]. It is also stable above 200 °C and at rather high vapour pressures, which is important for purification processes. The removal of chemical impurities does not only increase the light transmission but also the long-term stability of a metal loaded LS due to the fact that impurities could induce slow chemical reactions that cause the transparency of scintillator to deteriorate over time [64]. Therefore, the Gd was integrated into a molecule-complex, which increases the solubility in organic solvents. The MPIK Heidelberg initially considered ACAC (acetylacetonante) as ligand for the beta-diketonate-complex, but it was difficult to sublime and lacked the optical and radiochemical purity needed [63]. Therefore, the beta-diketonate was selected to be THD (2,2,6,6-tetramethyl-heptane-3,5-dionate). It proved to have a more effective shielding of the metal ions, which reduced the interaction between molecules and hydrolysis effects compared to ACAC.

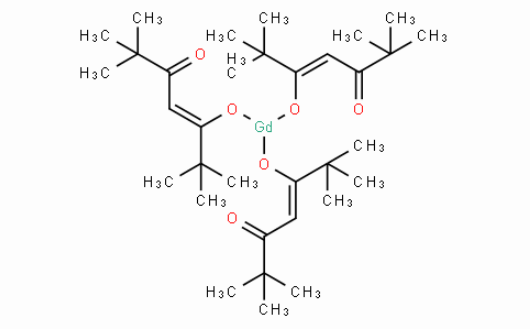

Figure 14.1: $Gd(thd)_3$ molecule [C28]

14.1 Double Chooz liquid scintillators

The target liquid scintillator (DC-Target) of Double Chooz consists of two solvents, n-dodecane and PXE, the primary fluor PPO and the secondary fluor bis-MSB (Table 14.1). PXE was chosen due to safety criteria but had to be diluted with n-dodecane to ensure compatibility with the acrylic vessels of the DC detectors. The Gd-concentration is about 0.1 $\%_{wt.}$, for which THF is needed to completely dissolve the $Gd(thd)_3$ powder. The Gd-loading in the DC-Target decreases the light yield due to the fact that $Gd(thd)_3$ is a quenching molecule. Therefore, the light yield of the Gamma Catcher (DC-GC) has to be lowered to match the light yield with the DC-Target. Also, the density of the two liquid scintillators has to be kept the same to ensure mechanical stability of the detector vessels. To meet these requirements, the DC-GC consists of three solvents: Mineral oil, n-dodecane and PXE. Furthermore, the PPO concentration is lower compared to the DC-Target, which makes the scintillation time slower, to allow separation between Target and GC events using pulse shape analysis.

Scintillator	Composition	Quantity
Target	n-dodecane	80 $\%_{vol}$
	PXE	20 $\%_{vol}$
	$Gd(thd)_3$	4.5 g/l
	Oxolane (tetrahydrofuran, THF)	0.5 $\%_{wt.}$
	PPO	7 g/l
	bis-MSB	20 mg/l
Gamma Catcher	Mineral oil	66 $\%_{vol}$
	n-dodecane	30 $\%_{vol}$
	PXE	4 $\%_{vol}$
	PPO	2 g/l
	bis-MSB	20 mg/l

Table 14.1: Composition of the Target and Gamma Catcher scintillator of Double Chooz [63].

14.2 STEREO liquid scintillators

To meet safety aspects when operating close to a nuclear reactor and compatibility with detector materials LAB was chosen as scintillator basis in the STEREO experiment. The main advantages of LAB compared to other solvents are the high transparency above 400 nm, low cost, high flash point and also that it is chemically rather inert [67]. To improve the PSD capability, PXE and DIN were added to the liquid scintillator mixture (Table 14.2). To reduce the rather high accidental background rate at ILL the Gd-concentration was almost doubled compared to Double Chooz (0.9 $\%_{\text{wt.}}$ of $Gd(thd)_3$ corresponds to 0.2 $\%_{\text{wt.}}$ of pure Gd). The primary fluor of the STEREO Target (ST-Target) is PPO and the secondary bis-MSB. The STEREO Gamma Catcher (ST-GC) is identical to the target, except the $Gd(thd)_3$ and THF are missing. Furthermore, the PPO concentration is lower (3 g/l) compared to the ST-Target. The reason is that the higher the Gd-to-primary-fluor ratio, the stronger the quenching and therefore the lower the light yield. Because of that the PPO concentration was chosen to be higher for the ST-Target than for the ST-GC. Pulse shape discrimination is used to discriminate correlated background in STEREO, mainly fast neutrons. Here, the prompt event is mimicked by recoil protons and the delayed event by neutron capture. But this kind of events can be identified due to the fact that recoil protons excite more triplet states of the solvent molecules than positrons and therefore the pulse has a longer decay time.

Scintillator	Composition	Quantity
Target	LAB	73.0 $\%_{\text{wt.}}$
	PXE	19.5 $\%_{\text{wt.}}$
	DIN	4.9 $\%_{\text{wt.}}$
	$Gd(thd)_3$	0.9 $\%_{\text{wt.}}$
	Oxolane (tetrahydrofuran, THF)	0.9 $\%_{\text{wt.}}$
	PPO	0.8 $\%_{\text{wt.}}$ (7 g/l)
	bis-MSB	0.002 $\%_{\text{wt.}}$ (20 mg/l)

Table 14.2: Composition of the Target scintillator of STEREO [67].

14.3 Gd-scintillator stability

Optical stability is an important basic requirement for reactor neutrino experiments that collect data over several years. In particular the stability of metal loaded liquid scintillator is and was a challenge in many neutrino experiments [64]. Therefore, I have measured the light yield of the Target and Gamma Catcher of Double Chooz and STEREO about 11 years (Double Chooz) and 5 years (STEREO) after production.

Mixture	**LY**	**rel. LY**	**FoM$_{max}$**	**rel. FoM$_{max}$**
EJ301	1133	1.296	2.357	1.997
PXE(4g/l PPO, 10mg/l POPOP)	941	1.077	1.224	1.037
LAB(4g/l PPO, 20mg/l POPOP)	874	1.000	1.180	1.000
ST-GC	749	0.857	1.216	1.031
ST-Target	575	0.658	1.430	1.212
DC-GC	196	0.224	-	-
DC-GC (2)	311	0.356	-	-
DC-Target	550	0.629	0.739	0.626

Table 14.3: Light yield of Target and Gamma catcher of DC and STEREO compared to LAB.

The light yield of the DC-Target compared to PXE was measured to be $57.6 \pm 1.0\%$ at the beginning of the Double Chooz experiment, and the DC-GC had 97% of the target light yield [63]. Our measurement shows that the DC-Target has compared to PXE $58.4 \pm 2.0\%$ of its light yield, which is in very good agreement with the old value. For the DC-GC I measured two different samples with about 36% and 57 %. Both values are much lower than expected. This could be explained by limitations in the storage conditions of the GC samples. There were no indications for any optical instabilities of the DC liquids during the 7 years of detector operation (see Figure 14.2).

For STEREO the light yield of the ST-Target after production was determined to be about 6500 ± 300 photons/MeV and 8400 ± 400 photons/MeV [67] for the ST-GC, which corresponds to an relative light yield of ST-Target to ST-GC of 1.292 ± 0.086. For comparison, we also measured EJ301, which has a light output compared to anthracene of 78% [C9]. Anthracene produces about 17400 photons/MeV [67]. With that we get 6900 ± 200 photons/MeV for ST-Target and 9000 ± 300 photons/MeV for ST-GC and therefore a relative light between target and GC of 1.304 ± 0.058 after the end of the experiment. Both measurements agree with the light yield measured at the start of the experiment within the error. In particular, the almost identical ratio of ST-Target to ST-GC measured after 5 years in a completely different setup is not worthy. Therefore the stability of optical properties, at least the light yield, of the Gd-liquid scintillators of Double Chooz and STEREO over multiple years could

be confirmed with these measurements.

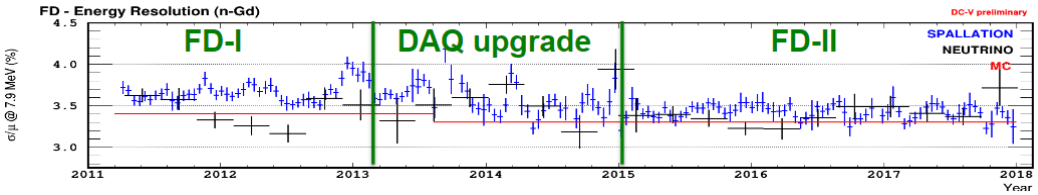

Figure 14.2: Energy resolution over time [57]. The x-axis shows the time from 2011 to 2018. The y-axis shows the deviation in energy resolution given in %, where the percent value is the standard deviation relative to the mean energy resolution at an energy of 7.9 MeV. No worsening of resolution could be observed over the full period of data collection.

Part VI

Conclusion

Organic liquid scintillators are an important tool for neutrino experiments like Double Chooz and STEREO. In many cases detection efficiency demands large size detector volumes with the extreme example of tens of thousands of cubic meters of liquid scintillator. In this framework, the issues connected with liquid toxicity, volatility and flammability of solvents are enhanced. Therefore, the demands of safe solvents increased in the last years. In this context, different scintillator compositions were studied. The light yield, PSD and attenuation length of the scintillator samples were measured and analysed with a self written macro. The light yield was measured with a ^{137}Cs source and the PSD with an AmBe source, each for five minutes. A new setup and DAQ system was used and tested for the first time for such type of measurements at MPIK. The scintillator samples were prepared and measured at the MPIK, Heidelberg. Three scintillator samples have to be highlighted: the DIN, LAB and phenylsiloxane based scintillators. Each of them has its strength in a different application.

A DIN based scintillator has a high light yield comparable to 1-Methylnaphthalene but distinguishes itself with a very good PSD capability from the others. Its disadvantages are the rather small attenuation length and the classification as hazardous for human health and harmful for the environment. A relative small detector, where the attenuation length and the hazards are acceptable and which needs a good energy resolution and pulse shape discrimination to differentiate between different ionizing particles would perfectly fit for a DIN based scintillator.

The LAB based scintillator on the other hand has a worse light yield and PSD than the DIN based one, but has a much larger attenuation length. It is similar to PXE in light yield and PSD but does not have the drawback of being harmful for the environment like PXE, 1-Methylnaphthalene and DIN. LAB is suitable for large detectors, which do not need such a high light yield and PSD. Examples for experiments using LAB as scintillator basis are SNO+, Daya Bay, RENO and JUNO.

The phenylsiloxane (S-04V) based scintillator has a similar light yield and PSD as LAB, but about half of the attenuation length. However, the attenuation length has much higher potential due to the fact that the phenylsiloxane was not purified and the chemical purity is unknown. Its major advantages are its very high flash point and very low vapour pressure, even compared to other safe scintillators. Moreover, it does not have a single GHS pictogram, it is chemical inert and simple to dispose. A phenylsiloxane based scintillator would perfectly fit a detector, for which safety is the most important criterium and energy resolution and pulse shape discrimination are rather of secondary importance.

With this new siloxane based scintillator, muon-flux measurements were performed in different laboratories at the MPIK. With a calibration measurement with ^{137}Cs the dominant background was identified to be potassium and thallium and a cut value could be defined for cosmic muons above a visible energy of 2.5 MeV deposited in the

scintillator. A measurement in the spectrometry lab at the window was performed, which corresponds to the muon-flux without shielding. Also, a measurement in the Low-Level-Lab was performed and the reduction factor was determined to be about 2.6 compared to the spectrometry lab. Three different positions at different heights were performed in the new laboratory room Ge166 at MPIK. The reduction factor compared to the spectrometry lab was determined to be between 1.38 to 1.71 depending on the position in the lab. This was expected due to the fact that one side of the laboratory, mainly from the hillside, has some overburden. Also, the neutron background could be estimated with a PSD cut. The measured reduction factors of the different labs were consistent with the muon reduction factors.

Finally, the stability of the DC and STEREO Gd-scintillator was studied. The stability of metal loaded liquid scintillator is and was a challenge in many neutrino experiments, but is crucial for data taking over several years. Therefore, the light yield of the Target and Gamma Catcher (GC) of Double Chooz (DC) and STEREO (ST) was measured after 11 years for Double Chooz and 5 years for STEREO after production.

The DC-Target had a light yield of $58.4 \pm 2.0\%$ compared to PXE, which is in very good agreement with measurements after production ($57.6 \pm 1.0\%$). The light yield of the DC-GC on the other hand was much lower than expected, which could be caused by storage conditions of the DC-GC samples. During the 7 years of detector operation there were no indications of any optical instabilities of the DC liquids.

For STEREO the ratio of the light yield of ST-Target to ST-GC was determined to be 1.304 ± 0.058, which is in very good agreement with the ratio measured after production of 1.292 ± 0.086. With these measurements the stability of optical properties, at least the light yield, of the Gd-liquid scintillators of Double Chooz and STEREO over multiple years could be confirmed.

Part VII

Appendix

A Light-yield-model

For the Light-yield-model [45] [12] describe a scintillator with two solvents that are the donors D_1 and D_2, a quenching molecule Q e.g. Gadolinium and one fluor that is the acceptors A_1.

A.1 Assumptions of the model

- The energy transfer processes are shown in Figure A.1 and the notation in Table A.1.
- All transfer rates are considered as time- and location-independent and proportional to the concentration of the involved molecule.
- The concentrations of the unexcited molecule are constant, which means time-independent. This assumption can be made due to the very large amount of molecules in comparison to the excited molecules.
- Direct excitation of the acceptors or quenching molecules are not taken into account due to the low impact.
- The quenching molecules do not contribute to the light yield due to the conversion into thermal energy. Also, energy is lost due to internal processes of the solvents and self quenching of the primary fluor.
- Spontaneous emission of photons by the solvents are neglected. The radiationless transfer of energy and internal losses are much more efficient.
- The transfer of energy from the primary solvent D_1 to the secondary solvent D_2 is not considered. The reason for that is that we presuppose that the emission spectrum of the primary solvent does not overlap with the absorption spectrum of the secondary solvent.

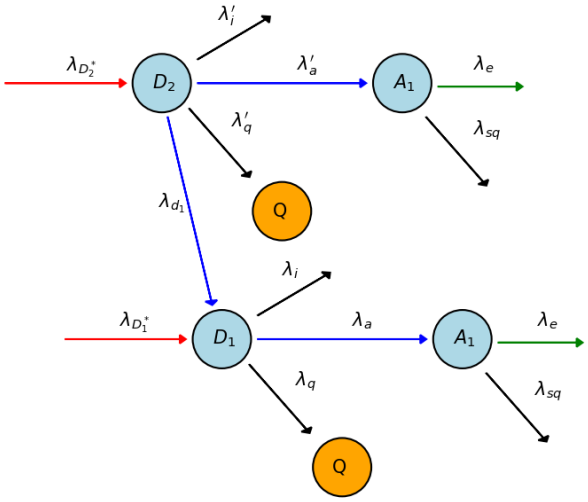

Figure A.1: Energy transfer processes: The black arrows are processes where energy is lost, blue arrows are processes with radiationless energy transfer, green processes are the de-excitation of the primary fluor by the emission of a photon and the red arrows are the excitation of the solvents by compton-electrons.

A.2 Determination of the light-yield-equation

First of all one has to look at how the concentrations of D_1^* ,D_2^* and A_1^* change over time.

$$\frac{dD_1^*}{dt} = \lambda_{D_1^*} - \lambda_a D_1^* A_1 - \lambda_i D_1^* - \lambda_q D_1^* Q + \lambda_{d_1} D_2^* D_1 \tag{A.1}$$

$$\frac{dD_2^*}{dt} = \lambda_{D_2^*} - \lambda'_a D_2^* A_1 - \lambda'_i D_2^* - \lambda'_q D_2^* Q - \lambda_{d_1} D_2^* D_1 \tag{A.2}$$

$$\frac{dA_1^*}{dt} = \lambda_a D_1^* A_1 + \lambda'_a D_2^* A_1 - \lambda_e A_1^* - \lambda_{sq} A_1 A_1^* \tag{A.3}$$

Symbol	Description	Physical quantity
D_1 , d_1	primary donor	$\frac{mol}{l}$, $\frac{g}{l}$
D_2 , d_2	secondary donor	$\frac{mol}{l}$, $\frac{g}{l}$
A_1 , a_1	primary fluor	$\frac{mol}{l}$, $\frac{g}{l}$
Q , q	quenching molecule	$\frac{mol}{l}$, $\frac{g}{l}$
$*$	excited molecule	-
M_{D_1}	molar mass of D_1	$\frac{g}{mol}$
M_{D_2}	molar mass of D_2	$\frac{g}{mol}$
M_{A_1}	molar mass of A_1	$\frac{g}{mol}$
M_Q	molar mass of Q	$\frac{g}{mol}$
λ_a , $k_a = \frac{\lambda_a}{M_{A_1}}$	energy transfer from D_1 to A_1	$\frac{l}{mol \cdot s}$, $\frac{l}{g \cdot s}$
λ_e , $k_e = \lambda_e$	emission of a photon of A_1	s^{-1}
λ_q , $k_q = \frac{\lambda_q}{M_Q}$	energy transfer from D_1 to Q	$\frac{l}{mol \cdot s}$, $\frac{l}{g \cdot s}$
λ_i , $k_i = \lambda_i$	internal losses of D_1	s^{-1}
λ_{sq} , $k_{sq} = \frac{\lambda_{sq}}{M_{A_1}}$	self-quenching of A_1	$\frac{l}{mol \cdot s}$, $\frac{l}{g \cdot s}$
λ', k'	definition of the same variables for D_2	-
λ_{d_1} , $k_{d_1} = \frac{\lambda_{d_1}}{M_{D_1}}$	energy transfer from D_2 to D_1	$\frac{l}{mol \cdot s}$, $\frac{l}{g \cdot s}$
$\lambda_{D_1^*}$	rate of the excitation of D_1	$\frac{mol}{l \cdot s}$
$\lambda_{D_2^*}$	rate of the excitation of D_2	$\frac{mol}{l \cdot s}$

Table A.1: Notation of the light-yield-model

With these three equations, one can determine D_1^* ,D_2^* and A_1^*.

$$D_1^* = \frac{1}{\lambda_a A_1 + \lambda_i + \lambda_q Q} \left[\lambda_{D_1^*} + \lambda_{d_1} D_2^* D_1 - \frac{dD_1^*}{dt} \right] \tag{A.4}$$

$$D_2^* = \frac{1}{\lambda'_a A_1 + \lambda'_i + \lambda'_q Q + \lambda_{d_1} D_1} \left[\lambda_{D_2^*} - \frac{dD_2^*}{dt} \right] \tag{A.5}$$

$$A_1^* = \frac{1}{\lambda_e + \lambda_{sq} A_1} \left[\lambda_a A_1 D_1^* + \lambda'_a A_1 D_2^* - \frac{dA_1^*}{dt} \right] \tag{A.6}$$

To get an equation for A_1, which does not depend on D_1^* and D_2^* one can replace D_2^* in Equation A.4 and then insert this new equation of D_1^* and Equation A.5 into Equation A.6.

$$\begin{aligned} A_1^* = & \frac{1}{\lambda_e + \lambda_{sq} A_1} \frac{\lambda_e A_1}{\lambda_a A_1 + \lambda_i + \lambda_q Q} \left[\lambda_{D_1^*} - \frac{dD_1^*}{dt} \right] \\ & + \frac{1}{\lambda_e + \lambda_{sq} A_1} \frac{\lambda_a A_1}{\lambda_a A_1 + \lambda_i + \lambda_q Q} \frac{\lambda_{d_1} D_1}{\lambda'_a A_1 + \lambda'_i + \lambda'_q Q + \lambda_{d_1} D_1} \left[\lambda_{D_2^*} - \frac{dD_2^*}{dt} \right] \\ & + \frac{1}{\lambda_e + \lambda_{sq} A_1} \frac{\lambda'_a A_1}{\lambda'_a A_1 + \lambda'_i + \lambda'_q Q + \lambda_{d_1} D_1} \left[\lambda_{D_2^*} - \frac{dD_2^*}{dt} \right] \end{aligned} \tag{A.7}$$

For the light yield, one wants to know the total amount of photons N_p emitted by the primary fluor:

$$N_p = \int_{-\infty}^{\infty} \lambda_e A_1^*(t) dt \tag{A.8}$$

Only the terms in square bracket in Equation A.7 depending on time, everything else is constant, which means one can solve the integration for each one separate.

The excitation of a molecule is very fast compared to the de-excitation processes. Because of that, one can assume that the excitation occur at $t = 0 \rightarrow \lambda_{D_{1,2}^*}(t) = D_{1,2}^0 \delta(t)$, where $\delta(t)$ is the Dirac-delta-function.

$$\int_{-\infty}^{\infty} \left[\lambda_{D_{1,2}^*}(t) - \frac{dD_{1,2}^*}{dt} \right] = D_{1,2}^0 + \underbrace{D_{1,2}(t=\infty)}_{=0} - \underbrace{D_{1,2}(t=-\infty)}_{=0} = D_{1,2}^0 \tag{A.9}$$

$D_{1,2}(t = \pm\infty) = 0$ because long times before and after the excitation are no excited molecules left. With these results, one can determine the total amounts of photons emitted from the primary fluor:

$$\begin{aligned} N_p = {} & D_1^0 \, \frac{1}{\lambda_e + \lambda_{sq} A_1} \, \frac{\lambda_e A_1}{\lambda_a A_1 + \lambda_i + \lambda_q Q} \\ & + D_2^0 \, \frac{1}{\lambda_e + \lambda_{sq} A_1} \, \frac{\lambda_a A_1}{\lambda_a A_1 + \lambda_i + \lambda_q Q} \, \frac{\lambda_{d_1} D_1}{\lambda_a' A_1 + \lambda_i' + \lambda_q' Q + \lambda_{d_1} D_1} \\ & + D_2^0 \, \frac{1}{\lambda_e + \lambda_{sq} A_1} \, \frac{\lambda_a' A_1}{\lambda_a' A_1 + \lambda_i' + \lambda_q' Q + \lambda_{d_1} D_1} \end{aligned} \tag{A.10}$$

One can determine the constants D_1^0 and D_2^0 by the different probabilities of the solvents to interact with electrons and the probability that this interaction leads to an excitation of the solvent. We assume that the electrons, mostly compton-electrons, lose all their energy by interactions with the two solvents. Then we only have to calculate the probability of an interaction of an electron with the solvent W_{D_1} and W_{D_2}.

$$W_{D_1} = \frac{\sigma_{D_1} n_{D_1}}{\sigma_{D_1} n_{D_1} + \sigma_{D_2} n_{D_2}} = \frac{\eta x_{D_1}}{\eta x_{D_1} + (1 - x_{D_1})} \tag{A.11}$$

$$W_{D_2} = 1 - \frac{\sigma_{D_1} n_{D_1}}{\sigma_{D_1} n_{D_1} + \sigma_{D_2} n_{D_2}} = \frac{1 - x_{D_1}}{\eta x_{D_1} + (1 - x_{D_1})} \tag{A.12}$$

where σ_{D_1} and σ_{D_2} are the cross sections of the solvents for an interaction with an electron, n_{D_1} and n_{D_2} are the particle densities of the solvents, $\eta = \frac{\sigma_{D_1}}{\sigma_{D_2}}$ and $x_{D_1} = \frac{n_{D_1}}{n_{D_1} + n_{D_2}}$. Therefore, we can express D_1^0 and D_2^0 as:

$$D_1^0 = N_0^{D_1} W_{D_1} \tag{A.13}$$

$$D_2^0 = N_0^{D_2} W_{D_2} \tag{A.14}$$

where $N_0^{D_1}$ and $N_0^{D_2}$ are the number of excited molecules pure D_1 solvent or D_2 solvent.

Finally, we want the concentration in units of g/l and express the light yield relative to a measured standard I. Therefore, we define new energy transfer constants k (Table A.1).

$$\begin{aligned} I_{LY} = I_0^{D_1} & \frac{\eta x_{D_1}}{\eta x_{D_1} + (1 - x_{D_1})} \frac{1}{1 + \frac{k_{sq} a}{k_e}} \frac{1}{1 + \frac{k_i}{k_a a} + \frac{k_q q}{k_a a}} \\ + I_0^{D_2} & \frac{1 - x_{D_1}}{\eta x_{D_1} + (1 - x_{D_1})} \frac{1}{1 + \frac{k_{sq} a}{k_e}} \frac{1}{1 + \frac{k_i}{k_a a} + \frac{k_q q}{k_a a}} \frac{1}{1 + \frac{k'_a a}{k_{d_1} d_1} + \frac{k'_i}{k_{d_1} d_1} + \frac{k'_q q}{k_{d_1} d_1}} \\ + I_0^{D_2} & \frac{1 - x_{D_1}}{\eta x_{D_1} + (1 - x_{D_1})} \frac{1}{1 + \frac{k_{sq} a}{k_e}} \frac{1}{1 + \frac{k'_i}{k'_a a} + \frac{k'_q q}{k'_a a} + \frac{k_{d_1} d_1}{k'_a a}} \end{aligned} \tag{A.15}$$

The final equation shows the three different possible energy paths. The first term is the excitation of the primary solvent with an energy transfer to the primary fluor, which then emits photons. The second term is the excitation of the secondary solvent with an energy transfer to the primary solvent, which then transfers its energy to the primary fluor, which finally emits the photons. The third term is the same term as the first, but for the second solvent.

A standard scintillator of one solvent and one fluor gives an simpler expression:

$$I_{LY} = I_0^{D_1} \frac{1}{1 + \frac{k_{sq} a}{k_e}} \frac{1}{1 + \frac{k_i}{k_a a}} \tag{A.16}$$

B Lists

B.1 List of Figures

B.2 List of Tables

C Bibliography

[1] H. Kolanoski, N. Wermes, Teilchendetektoren Grundlagen und Anwendungen, Springer (2016) chapter 13.

[2] A. De Angelis & M. Pimenta, Introduction to Particle and Astroparticle Physics (2nd Edition), Springer (2018) chapter 4.

[3] C. Aberle, Optimization, simulation and analysis of the scintillation signals in the Double Chooz experiment, Dissertation, University of Heidelberg (2011).

[4] P. Rinard, Neutron Interactions with Matter, Los Alamos National Laboratory (n.d.).

[5] F. Hinderer, UV/Vis-Absorptions und Fluoreszenz Spektroskopie, Einführung in die spektroskopische Analyse mit UV- und sichtbarer Strahlung, Springer Spektrum (2020) chapter 7.

[6] H. Pohl, What is the difference between fluorescence, phosphorescence and luminescence?, https://www.enzolifesciences.com/science-center/technotes/2019/december/what-is-the-difference-between-fluorescence-phosphorescence-and-luminescence (2019).

[7] C. Aberle, Optimierung der Fluoreszenzcharakteristik von Flüssigkeitszintillatoren des Double Chooz Reaktorneutrinoexperiments, diploma thesis (2008) MPIK Heidelberg.

[8] O. Stern & M. Volmer, Über die Abklingungszeit der Fluoreszenz, Physik. Z. (1919) 20.

[9] F. Perrin, Compte Rendue 178 (1924).

[10] Th. Förster, Zwischenmolekulare Energieumwandlung und Fluoreszenz, Annalen der Physik (1948).

[11] H. Kallmann & M. Furst, Fluorescence of Solutions Bombarded with High Energy Radiation (Energy Transport in Liquids), Phys. Rev. 79 (1950) 857.

[12] C. Aberle, Optimierung der Fluoreszenzcharakteristik von Flüssigkeitszintillatoren des Double Chooz Reaktorneutrinoexperiments, Diplomarbeit page 35-40 (2008) MPIK Heidelberg.

[13] CDC, Radioisotope Brief: Caesium-137 (Cs-137), https://www.cdc.gov/nceh/radiation/emergencies/isotopes/cesium.htm (2018).

[14] M. A. Ashraf, Caesium-137: Radio-Chemistry, Fate, and Transport, Remediation, and Future Concerns, Critical Reviews in Environmental Science and Technology (2014).

[15] Table of Radioactive Isotopes, Caesium-137, http://nucleardata.nuclear.lu.se/toi/nuclide.asp?iZA=550137 (2021).

[16] J.Scherzinger, J.R.M.Annand, G.Davatz & more, Tagging fast neutrons from an ^{241}Am/^{9}Be source, Applied Radiation and Isotopes 98 (2015).

[17] H.A. Molina, Evaluation of the neutron detection efficiency in the Stereo reactor neutrino experiment, Dissertation (2020) MPIK Heidelberg.

[18] Hamamatsu Photonics K.K, Photomultiplier Tubes – Basics and Applications (3rd Edition) (2007).

[19] L. Huth, Charakterisierung der Double Chooz–Photomultiplier, Bachelorarbeit (2012) MPIK Heidelberg.

[20] P. Lombardi, F. Ortica, G. Ranucci, A. Romani, Decay time and pulse shape discrimination of liquid scintillators based on novel solvents, Nucl.Instrum.Meth.A 701 (2013) 133-144.

[21] T. Marrodan Undagoitia, F. von Feilitzsch, L. Oberauer, W. Potzel, A. Ulrich, J. Winter, and M. Wurm, Fluorescence decay-time constants in organic liquid scintillators, Rev. Sci. Instr. 80, 043301 (2009).

[22] CAEN, User Manual UM4380 - 725-730 DPP-PSD Registers (Rev. 5) (2018).

[23] CAEN, Guide GD6300 - CoMPASS Quick Start (Rev. 11) (2020).

[24] CONUS Collaboration, Neutron-induced background in the CONUS experiment, Eur.Phys.J.C 79 (2019) 8, 699.

[25] CAEN, V1725 / V1725S, https://www.caen.it/products/v1725/ (2021).

[26] M. Gudino, Engineering Resources: Basics of Analog-to-Digital Converters, https://www.arrow.com/en/research-and-events/articles/engineering-resource-basics-of-analog-to-digital-converters (2018).

[27] IEC, dynamic range, https://www.electropedia.org/iev/iev.nsf/display?openformievref=723-03-11 (1997).

[28] K. Carnes, Constant Fraction Discriminators, https://jrm.phys.ksu.edu/Resource/Pubs/CFD/CFD.html (2003).

[29] M.J. Safari, F. Abbasi Davani, H. Afarideh, Differentiation method for localization of Compton edge in organic scintillation detectors, arXiv:1610.09185 (2016).

[30] Borexino Collaboration, Pulse-Shape discrimination with the Counting Test Facility, Nucl.Instrum.Meth.A584:98-113 (2008).

[31] C. Buck, B. Gramlich, M. Lindner, C. Roca and S. Schoppmann, Production and properties of the liquid scintillators used in the Stereo reactor neutrino experiment, JINST 14 (2019) 01, P01027.

[32] ROOT Cern, Chapter: Trees, https://root.cern.ch/root/htmldoc/guides/users-guide/Trees.html (2021).

[33] Borexino Collaboration, Measurement of geo-neutrinos from 1353 days of Borexino, Phys.Lett.B 722 (2013) 295-300.

[34] T. Araki et al., KamLAND Collaboration, Experimental investigation of geologically produced antineutrinos with KamLAND, Nature 436 (2005) 499–503.

[35] Merriam-Webster, flash point, https://www.merriam-webster.com/dictionary/flash%20point (2021).

[36] Perkin Elmer, Liquid Scintillation Cocktails, https://www.perkinelmer.com/de/lab-products-and-services/application-support-knowledgebase/radiometric/liquid-scintillation-cocktails.html (2021).

[37] M.C. Chen, The SNO liquid scintillator project, Nucl.Phys.B Proc.Suppl. 145 (2005) 65-68.

[38] Daya Bay Collaboration, Observation of electron-antineutrino disappearance at Daya Bay, Phys.Rev.Lett. 108 (2012) 171803.

[39] RENO Collaboration, Observation of Reactor Electron Antineutrino Disappearance in the RENO Experiment, Phys.Rev.Lett. 108 (2012) 191802.

[40] JUNO Collaboration, Neutrino Physics with JUNO, J.Phys.G 43 3 (2016) 030401.

[41] Merriam-Webster, isomer, https://www.merriam-webster.com/dictionary/isomer (2021).

[42] H. Ross, J.E. Noakes, J.D. Spaulding, LIQUID SCINTILLATION COUNTING and ORGANIC SCINTILLATORS, LEWIS PUBLISHERS, INC (1991).

[43] C. Buck, B. Gramlich and S. Schoppmann, Novel Opaque Scintillator for Neutrino Detection, JINST 14 (2019) 11, P11007.

[44] C. Buck, B. Gramlich and S. Wagner, Light propagation and fluorescence quantum yields. in liquid scintillators, JINST 10 (2015) 09, P09007.

[45] C.Aberle, C.Buck, F.X.Hartmann, S.Schönert, Light yield and energy transfer in a new Gd-loaded liquid scintillator, Chem.Phys.Lett. 516 (2011) 257-262.

[46] I. B. Berlman, Handbook of fluoresence spectra of aromatic molecules (2nd edition) (1971).

[47] G. Goldstein, W.S. Lyon, Liquid Scintillators Using 1-Methylnaphthalene, Appl. Radiat. Isot. Vol. 13 (1964) 133-137.

[48] M.D. Palma, S.M. Carturan & more, Non-toxic liquid scintillators with high light output based on phenyl-substituted siloxanes, Optical Materials Volume 42 (2015) Pages 111-117.

[49] M.D. Palma, Polysiloxane based neutron detectors, Dissertation, University of Trento, Department of Industrial Engineering (2016).

[50] M.D. Palma et al., Pulse Shape Discrimination in Polysiloxane-Based Liquid Scintillator, IEEE TRANSACTIONS ON NUCLEAR SCIENCE, VOL. 63 (2016) NO. 3.

[51] A. F. Seliman, V.N. Bliznyuk, S. M. Husson and T. A. DeVol, Development of polymerizable 2-(1-naphthyl)-5- phenyloxazole scintillators for ionizing radiation detection, J. Mater. Chem. C 3 (2015) 7053-7061.

[52] Table of Radioactive Isotopes, ^{40}K , http://nucleardata.nuclear.lu.se /toi/nuclide.asp?iZA=810208 (2021).

[53] Table of Radioactive Isotopes, ^{208}Tl, http://nucleardata.nuclear.lu.se /toi/nuclide.asp?iZA=810208 (2021).

[54] G. Heusser, Cosmic ray-induced background in Ge-spectrometry, Nuclear Instruments and Methods in Physics Research B 83 (1993) 223-228.

[55] Double Chooz Collaboration, Letter of Intent for Double-CHOOZ: a Search for the Mixing Angle θ_{13}, e-Print: hep-ex/0405032 (2004).

[56] Double Chooz Collaboration, Double Chooz θ_{13} measurement via total neutron capture detection, Nature Phys. 16 (2020) 5, 558-564.

[57] C. Buck, New Results from the Double Chooz Experiment, https://zenodo.org/record/1286844.YWBELO1R2Uk (2018).

[58] S.E. Klett, Evolution of the Energy Calibration Coefficients in the Stereo Experiment, Bachelor Thesis at MPIK Heidelberg (2017).

[59] Stereo, The Stereo Experiment, https://www.stereo-experiment.org/public.php (2021).

[60] Stereo Collaboration, Sterile Neutrino Constraints from the STEREO Experiment with 66 Days of Reactor-On Data, Phys.Rev.Lett. 121 (2018), 161801.

[61] STEREO Collaboration, The STEREO Experiment, JINST 13 (2018), P07009.

[62] STEREO Collaboration, Improved sterile neutrino constraints from the STEREO experiment with 179 days of reactor-on data, PHYSICAL REVIEW D 102 (2020) 052002.

[63] MPIK Heidelberg, Large scale Gd-beta-diketonate based organic liquid scintillator production for antineutrino detection, JINST 7 (2012) P06008.

[64] C. Buck and M. Yeh, Metal-loaded organic scintillators for neutrino physics, J. Phys. G: Nucl. Part. Phys. 43 (2016) 093001.

[65] Apollonio M et al, Search for neutrino oscillations on a long base-line at the CHOOZ nuclear power station Eur. Phys. J. C 27 (2003) 331–74.

[66] F. Boehm, Results from the Palo Verde neutrino oscillation experiment, Phys. Rev. D 62 (2000) 072002.

[67] C. Buck, B. Gramlich, M. Lindner, C. Roca, S. Schoppmann, Production and properties of the liquid scintillators used in the STEREO reactor neutrino experiment, JINST 14 (2019) 01, P01027.

C.0.1 Chemicals

[C1] Merck, structure-search, https://www.sigmaaldrich.com./DE/en/structure-search (2021).

[C2] Merck, p-Xylene, https://www.merckmillipore.com/DE/en/product /p-Xylene,MDA_CHEM-808691, MSDS: https://www.merckmillipore.com/DE /en/product/msds/MDA_CHEM-808691?Origin=PDP (2021).

[C3] Merck, 1,2,4-Trimethylbenzene, https://www.merckmillipore.com/DE/en /product/124-Trimethylbenzene,MDA_CHEM-814505, MSDS: https://www. merckmillipore.com/DE/en/product/msds/MDA_CHEM-814505?Origin=PDP (2021).

[C4] Sigma-Aldrich, 2,5-Diphenyloxazol, https://www.sigmaaldrich.com/DE/en /substance/25diphenyloxazole2212592717?context=product, MSDS: https://www.sigmaaldrich.com/DE/en/sds/aldrich/d210404 (2021).

[C5] Sigma-Aldrich, 1,4-Bis-(5-phenyl-2-oxazolyl)-benzol, https://www.sigma aldrich.com/DE/en/product/sigma/p3754?context=product, MSDS: https://www.sigmaaldrich.com/DE/en/sds/sigma/p3754 (2021).

[C6] Sigma-Aldrich, 1,4-Bis-(2-methylstyryl)-benzol, https://www.sigma aldrich.com/DE/en/substance/14bis2methylstyrylbenzene 3104313280610?context=product, MSDS: https://www.sigmaaldrich.com /DE/en/sds/sigma/15090 (2021).

[C7] Merck, 2-Propanol, https://www.merckmillipore.com/DE/en/product /2-Propanol,MDA_CHEM-109634 (2021).

[C8] Merck, Cyclohexane, https://www.merckmillipore.com/DE/en/product /Cyclohexane,MDA_CHEM-102822 (2021).

[C9] Eljen Technology, NEUTRON/GAMMA PSD EJ-301, EJ-309.https://eljentechnology.com/products/liquid-scintillators/ej-301-ej-309 (2021).

[C10] Saint-Gobain, BC-501A, BC-519. https://www.crystals.saint-gobain.com/products/bc-501a-bc-519 (2021).

[C11] Cepsa, Material Safety Data Sheet (LAB), CAS-Number: 67774-74-7 (2016).

[C12] Rütgers, Sicherheitsdatenblatt CAS-Number: 38640-62-9 (2014).

[C13] Dixie Chemical Company, Inc., SAFETY DATA SHEET PXE, CAS-Number: 6196-95-8 (2012).

[C14] Guidechem, Benzene, C10-13-alkylderivs., https://www.guidechem.com/encyclopedia /benzene-c10-13-alkylderivs–dic235610.html (2021).

[C15] G. Collin, H. Höke, H. Greim, Naphthalene and Hydronaphthalenes in Ullmann's Encyclopedia of Industrial Chemistry, Wiley-VCH Verlag GmbH Co. KGaA (2003).

[C16] Richfortunechem, Phenyl xylyl ethane, http://www.richfortunechem.com/index.php?action=newsid=761 (2021).

[C17] Chemspider, 2,6-Di-iso-propylnaphthalene, http://www.chemspider.com/Chemical-Structure.29899.html (2021).

[C18] Perkin Elmer, Ultima Gold F, 2x5L. https://www.perkinelmer.com/product/ultima-gold-f-2x5-l-6013179 (2021).

[C19] Sigma Aldrich, 2-(4-Biphenyl)-5-phenyloxazol, https://www.sigmaaldrich.com/DE/en/sds/aldrich/216984 (2021).

[C20] Sigma Aldrich, 2-(4-Biphenylyl)-5-phenyl-1,3,4-oxadiazol, https://www.sigmaaldrich.com/DE/en/sds/aldrich/257850 (2021).

[C21] Sigma Aldrich, 2-(4-tert.-Butylphenyl)-5-(4-biphenylyl)-1,3,4-oxadiazol, https://www.sigmaaldrich.com/DE/en/sds/sigma/b8378 (2021).

[C22] Merck, Pyridine-2,6-dicarboxylic acid, https://www.merckmillipore.com/DE/en /product/msds /MDA_CHEM-800614?Origin=SERP (2021).

[C23] Thermo Fisher Scientific, SAFETY DATA SHEET 1-Methylnaphthalene, CAS-Number: 90-12-0 (2021).

[C24] Thermo Fisher Scientific, Product Specification A15327 1-Methylnaphthalene, 96%, CAS-Number: 90-12-0 (2021).

[C25] abcr, AB109386 | CAS 9005-12-3., Polymethylphenylsiloxane, viscosity 500 cSt (2021).

[C26] Sindlhauser, Products Vacuum pump oil and grease, S-04V and S-05V (2021).

[C27] Sigma Aldrich, 2-(1-Naphthyl)-5-phenyl-oxazol, https://www.sigmaaldrich.com/DE/de/product/SIGMA/N0251, MSDS: https://www.sigmaaldrich.com/DE/en/sds/sigma/n0251 (2021).

[C28] CATSYN, Tris(2,2,6,6-tetramethyl-3,5-heptanedionato)gadolinium(III) CAS 14768-15-1, http://www.catsyn.com/product/14768-15-1.html (2021).

Erklärung

Ich versichere, dass ich diese Arbeit selbstständig verfasst und keine anderen als die angegebenen Quellen und Hilfsmittel benutzt habe.

Heidelberg, den 29.10.2021,